Regulatory landscapes and structural choreography of transcription initiation in spirochetes

Vilma K. Trapp[1,†], Tingting Wang[2,†], Tarek Hilal[2], Janne J. Makinen[1,#], Juho Kotikoski[1], Paavo J. Tavi[1], Ville Levola[1], Sari Paavilainen[1], Bernhard Loll[2], Markus C. Wahl[2,3,*], Georgiy A. Belogurov[2,*]

[1] University of Turku, Department of Life Technologies, 20014 Turku, Finland

[2] Freie Universität Berlin, Institute of Chemistry and Biochemistry, Laboratory of Structural Biochemistry, Takustr. 6, 14195 Berlin, Germany

[3] Helmholtz-Zentrum Berlin für Materialien und Energie, Macromolecular Crystallography, Albert-Einstein-Str. 15, 12489 Berlin, Germany

[†] Shared first authors; these authors contributed equally to this work.

[#] Present address: Bioproton Europe OY, Rapulankatu 2, 20780 Kaarina, Finland

* Correspondence to: markus.wahl@fu-berlin.de; gebelo@utu.fi

Summary

Spirochaetota is a deeply rooted bacterial phylum of evolutionary and medical importance. We show that the spirochetal RNA polymerase (RNAP) has a diminished ability to melt promoters compared to its *Escherichia coli* counterpart. This deficiency is compensated by CarD and is not linked to the phylum's natural resistance to the antibiotic rifampicin. CryoEM analysis revealed that the spirochetal RNAP disengages the -35 element during promoter unwinding, which contrasts with other bacterial RNAPs that release this element later during the initial transcription. Our research also details the unusually tight, non-sequence-specific binding of the spirochetal RNAP holoenzyme to DNA, which may be linked to the highly extended structure of the spirochetal nucleoid. We support these observations with a structural analysis of the dimeric holoenzyme non-specifically bound to DNA. Our results highlight the functional diversity of bacterial transcription systems and lay the foundation for understanding transcription regulation in pathogenic spirochetes.

Introduction

RNA polymerase (RNAP) carries out an essential and most regulated step in gene expression, the synthesis of an RNA copy of the template DNA. All cellular RNAPs are multi-subunit enzymes that share homologous catalytic cores. Bacteria possess a single RNAP that is composed of five core subunits ($\alpha\alpha\beta\beta'\omega$) [1]. This multi-subunit core is guided to promoters by a dissociable subunit known as sigma (σ) factor [2]. A σ factor binds core RNAP subunits forming a holoenzyme complex. A holoenzyme containing the primary σ factor initiates transcription at promoters that contain conserved sequence elements centered at -35 and -10 relative to the transcription start site (TSS). However, most bacteria also possess alternative σ factors directing the RNAP core to specific subsets of promoters.

In the widely studied *E. coli* system, the primary RNAP holoenzyme melts promoter DNA very efficiently [3]. Consequently, regulation of promoter activity primarily occurs during recruitment [4,5] or through negative modulation of promoter melting by transcription regulator DksA [6,7] (**Figure 1A**). In contrast, primary holoenzymes from Mycobacteria have reduced DNA melting capacities compared with the *E. coli* system [8–10] and necessitate allosteric activators CarD [10–12] and RbpA [13–15] for efficient melting of promoters. Holoenzymes containing alternative σ factors also rely on positive allosteric regulators to facilitate promoter DNA melting [16,17].

It is not precisely known why the primary holoenzyme from *E. coli* melts promoters more efficiently than its counterparts from Bacilli (e.g. *Bacillus subtilis*) and Mycobacteria (e.g. *Mycobacterium tuberculosis*). The difference is not attributable to the σ subunit [10,18] but may be linked to a lineage-specific insertion 3 (Si3) in the β' subunit that enhances the stability of open promoter complexes (RPo) formed by *E. coli* holoenzyme [19]. Lineage-specific insertions are additional domains that are present in some RNAPs and not others (**Figure 1B**). Both Si3 and the lineage-specific sequence insertion 1 (Si1) are also important for the modulation of the promoter melting by transcription regulator DksA [20–23].

To broaden our understanding of transcription initiation in bacteria we performed a detailed biochemical and structural characterization of the RNAP holoenzyme from *Spirochaeta africana*, a free-living bacterium from the phylum Spirochaetota. This diderm bacterial phylum represents the most basal lineage within the Pseudomonadati kingdom (**Figure 1C**) [24] and is notable for a unique combination of basal transcription factors and lineage-specific insertions in RNAP subunits (**Figure 1D**). Spirochaetota are also characterized by their distinctively long and thin morphology and a periplasmic flagellum. A key unresolved question in spirochetal biology is how cellular components, including the transcription apparatus, are trafficked along their highly elongated body (~1:100 width-to-length ratio).

We show by biochemical analysis that the spirochetal holoenzyme has diminished ability to melt promoters compared to *E. coli* and displays unusually tight non-sequence-specific association with DNA. We present cryoEM-based structural analyses of *S. africana* RNAP that reveal novel DNA binding modes: a disengagement of the -35 promoter element upon RPo formation and a non-sequence-specific engagement of the DNA minor groove by a dimeric holoenzyme. These findings broaden our understanding of bacterial transcription, offer insights into the mechanism of promoter escape and suggest phylum-level variations in how transcription machinery navigates the bacterial nucleoid.

Results

In vitro reconstituted transcription system of *S. africana*

Spirochetes processes both positive and negative regulators of ribosomal RNA transcription, CarD and DksA, respectively [25]. Both CarD and DksA are measurably transcribed in *S. africana* (**Figure S1A**). While Spirochaetota are not unique in possessing

both factors, the interplay of the two factors has not been investigated in detail previously. We cloned and heterologously expressed *S. africana* RNAP, primary σ factor, CarD and DksA in *E. coli*. We hand-picked six *S. africana* promoters of various strengths (**Figure S1B**) and constructed transcription templates (**Figure 2A**). We then used the above components to reconstitute multi-round transcription by *S. africana* RNAP *in vitro*. In a small subset of experiments for comparative purposes we also employed RNAP purified directly from *S. africana* cells by a combination of chromatographic techniques.

S. africana is a fermentative halo-alkaliphilic bacterium that grows optimally at pH between 9 and 10 and is dependent on sodium for growth [26]. Most membrane pumps are annotated as sodium pumps suggesting sodium is used as a primary coupling ion, and cytoplasmic pH regulation is absent or inefficient [25]. Our early experiments revealed that transcription activity of *S. africana* RNAP at pH 9.0 is approximately threefold higher than at pH 7.5. Accordingly, most *in vitro* transcription experiments with *S. africana* RNAP were performed at pH 9.0, 11 mM $MgCl_2$ and total ionic strength of ~180 mM. Unlike *Borrelia* RNAP [27], both heterologously expressed and fully native *S. africana* enzymes did not require Mn^{2+} for activity (**Figure S2**).

To monitor transcription activity, we used a multi-round assay where a preformed holoenzyme was added to a linearized plasmid encoding a transcription unit consisting of a spirochetal promoter followed by a 0.7 kb transcript encoding Broccoli fluorogenic light up aptamer (FLAP) upstream of the terminator (**Figure 2B**) [28]. In most experiments we used 50 nM of DNA template, 1 μM of holoenzyme and relatively strong promoters. In such systems, *S. africana* RNAP produces up to 600 nM RNA in 10 min allowing for monitoring of transcription output by measuring FLAP fluorescence, estimation of transcription yield using RNA-specific fluorescent dyes (Qubit fluorometer and kits), and visualization of the transcript in denaturing PAGE using SYBR Gold staining (**Figure 2C**). FLAP fluorescence offered the best sensitivity and selectivity and was therefore employed as the main method throughout the study.

Throughout this study, we mainly report transcriptional activities in arbitrary fluorescence units, which suffice for the assessment of relative changes in transcription yield. Comparisons of FLAP and Qubit readings (**Figure 2C**) suggest a conversion factor of 1.7 to express these units in nM of RNA. However, a portion of transcripts map outside the target transcription unit (**Figure S3**), implying a slightly smaller multiplier.

Consistent with this, purified P-gre RNA, transcribed from a PCR-amplified short DNA template with minimal flanking DNA outside the transcription unit, indicates a coefficient of 1.4 for our instrumental setup [28]. This coefficient allows for the estimation of absolute promoter activities in our *in vitro* assays. For instance, *S. africana* and *E. coli* holoenzymes initiate approximately once per minute at their cognate rRNA promoters at 37 °C. This is 60-fold lower than one initiation per second estimated for *E. coli* holoenzyme at rrnB P1 *in vivo* [29] possibly due to the presence of additional activators like Fis *in vivo* [30] as well as broader effects of genomic context.

***S. africana* CarD stimulates promoters with suboptimal discriminators**

We selected six promoters with diverse sequences and varying strengths by searching the *S. africana* genome with promoter patterns and considering *in vivo* transcript levels (**Figure S1B**). These promoters featured a TTGACN -35 element, a 16-18 bp spacer, a TANNNT -10 element, a 6-7 bp discriminator, and an A or G at TSS (**Figure 2A**). We predicted TSS assuming initiation at a purine 6 bp from the -10 promoter element, or purine 7 bp away if the former was absent. We also mapped TSS by sequencing *in vitro* produced RNAs with Oxford Nanopore after ligating a 24 nt RNA adapter to the 5′ end. The RNA sequencing experiment confirmed the primary TSS but also indicated occasional slippage during transcription initiation at 5′-AAA (P-pori) and 5′-ACA (P-trna, P-fla) sequences (**Figure S4**).

S. africana RNAP initiated relatively efficiently at the P-gre, P-pori, and P-fla promoters irrespective of the presence of CarD (**Figure 2D**). We designated these promoters as robust. CarD attenuated robust promoters up to 1.5 fold. *S. africana* holoenzyme alone initiated inefficiently at P-prs, P-trna, P-rrna but in the presence of CarD the activity of these three promoters was same or higher than that of robust promoters. We designated these promoters as tunable. While most measurements were performed at 10 μM CarD to ensure saturation, 1 μM of CarD was sufficient for the full effect of CarD at P-gre and P-rrna promoters (**Figure 3A**).

Robust promoters feature discriminators that are more purine and AT-rich than those of tunable promoters, suggesting that the former are easier to melt than the latter (**Figure 2A**). At the same time, CarD effects did not correlate with the spacing between the -35 and -10 elements, as it activated P-rrna with a consensual 17 bp spacer while attenuating P-pori that also features a 17 bp spacer. Similarly, the presence or absence of an extended -10 element did not determine CarD action; P-trna (with the element) was

activated, whereas P-gre (also with the element) was attenuated. Overall, the spirochetal holoenzyme closely resembled the properties of its mycobacterial counterpart [10–12,31]. Adhering to its established role as an rRNA transcription regulator in Mycobacteria [31], spirochetal CarD significantly enhanced transcription from a spirochetal rRNA promoter.

S. africana DksA is a pH-dependent negative regulator of transcription

When tested at pH 9.0, *S. africana* DksA did not affect transcription initiation at four tested promoters, regardless of the presence of CarD (**Figure 2D**). However, DksA inhibited transcription 2-3-fold at all six promoters when tested at pH 7.5 (**Figure 2E-F**). When present, CarD protected four out of six promoters from inhibition by DksA, but P-rrna and to some extent P-pori remained sensitive to DksA. As a result, in the presence of CarD, DksA specifically inhibited P-rrna and P-pori promoters. At pH 7.5, 1 μM of DksA added to 0.5 μM holoenzyme was sufficient for the maximal extent of inhibition of P-rrna transcription (**Figure 3B**). A higher concentration of DksA (5-10 μM) was required to inhibit P-rrna twofold at pH 8.0, and at pH 8.5, the DksA effect on P-rrna transcription was mostly absent. Additionally, the alarmone ppGpp did not stimulate inhibition of P-rrna by DksA at pH 8.0 (**Figure 3C**), although ppGpp did strongly stimulate inhibition of transcription from rrnB P1 by *E. coli* RNAP with *E. coli* DksA in a control experiment (**Figure 3D**). Overall, our data indicate that *S. africana* DksA is a potent negative regulator of transcription initiation, that in the presence of CarD acts only at certain promoters, such as the rRNA promoter. Although *S. africana* does not grow below pH 8.0, a culture pre-grown at pH 9.2 remains viable for several days at pH 7.5 at 25 °C: most cells retain their spiral shape, stay motile and resume growth when transferred back to the alkaline medium (**Video S1**). These observations indicate that the transcription activity of *S. africana* DksA at pH 8 and below may be physiologically relevant.

Stimulation by CarD is not linked to rifampicin resistance

Rifampicin resistance is a distinctive characteristic of spirochetal RNAP [32]. This led us to investigate whether this resistance contributes to inefficient initiation at certain promoters, making spirochetal RNAPs reliant on CarD. Bioinformatic analysis suggested that rifampicin resistance in spirochetes is due to the strict conservation of the Asn residue (βAsn490 in *S. africana* RNAP) at a specific position in the β subunit [33]. In contrast, most other bacterial phyla have a Ser residue at this position (βSer531 in *E.*

coli RNAP). To test this idea, we constructed a βN490S variant of *S. africana* RNAP and a βS531N variant of *E. coli* RNAP and examined their sensitivity to rifampicin. Wild-type *S. africana* RNAP was completely resistant to 1 μM rifampicin, whereas transcription by the βN490S variant was strongly inhibited by 1 μM rifampicin (**Figure 4A**). Conversely, 1 μM rifampicin completely abolished transcription by the wild-type *E. coli* RNAP but had no effect on transcription by the βS531N variant (**Figure 4B**). These results demonstrate that the phylum-specific Asn residue is the primary determinant of rifampicin resistance in Spirochaetota.

We then compared the performance of the wild-type and variant holoenzymes on a set of four *S. africana* promoters. The results showed a negligible effect of βN490S on *S. africana* holoenzyme activity, with only marginal changes observed at P-rrna and P-trna promoters (<1.5 fold) (**Figure 4C**). Additionally, the βN490S substitution did not impact the effects of CarD at P-rrna and P-gre promoters. Similarly, the βS531N substitution had a minimal effect on *E. coli* holoenzyme activity at *S. africana* promoters (**Figure 4D**). However, βS531N substitution significantly (3-fold) impaired the ability of *E. coli* holoenzyme to initiate at *E. coli* rrnB P1.

CarD aligns promoter preferences of *S. africana* and *E. coli* holoenzymes

Next, we compared the activity of *S. africana* and *E. coli* holoenzymes using a full set of six *S. africana* promoters. To speed up data acquisition, we used an end-point-only implementation of the FLAP assay. Transcription reactions were performed for 10 min in a thermoblock, quenched with a fluorogen-EDTA mixture followed by fluorescence measurements. In the absence of CarD, the relative promoter preferences of *E. coli* (**Figure 4E**, gray) and *S. africana* holoenzymes (**Figure 4F**, cyan) were significantly different. *E. coli* holoenzyme displayed high activity at tunable promoters (P-prs, P-trna, P-rrna) where the basal activity of *S. africana* holoenzyme is low but performed poorly at robust promoters (P-gre, P-pori) where the basal activity of *S. africana* holoenzyme is high. Only P-fla displayed high activity with both holoenzymes. CarD made *S. africana* holoenzyme more similar to its *E. coli* counterpart by activating tunable promoters and slightly attenuating robust promoters (**Figure 4F**, magenta). Interestingly, 10% DMSO, known to facilitate DNA melting, closely mimicked the effect of CarD on the spirochetal holoenzyme across all promoters and established even better alignment of promoter preferences between *S. africana* and *E. coli* holoenzymes (**Figure 4F**, blue). These

observations suggest that the spirochetal holoenzyme has intrinsically lower capacity to melt promoters than the *E. coli* enzyme, and this deficiency is compensated by CarD.

We then investigated whether a modified *E. coli* holoenzyme lacking Si3 inserts, known to form an unstable RPo [19], would exhibit reduced activity at tunable promoters. Contrary to the expectations, ΔSi3 *E. coli* holoenzyme displayed similar promoter preferences and absolute activity to the wild-type *E. coli* holoenzyme (**Figure 4E**). These findings indicate that the Si3 insert and RPo stability do not significantly influence transcription initiation in our high-NTP assays (1 mM of each NTP). Therefore, differences in promoter melting capacity between *S. africana* and *E. coli* RNAP are related to the forward rate of promoter melting [11], not the stabilization of the melted state.

Structure of *S. africana* RPo: the transcription bubble and CarD

To illuminate the structural choreography of transcription initiation in spirochetes we determined the cryoEM structures of promoter complexes formed by *S. africana* RNAP holoenzyme at P-rrna and P-gre promoters in the presence of CarD at the overall resolution of about 3 Å (**Table S2**). For the P-gre promoter, we also determined the structure in the absence of the factor. Unsurprisingly, the overall structures of *S. africana* RPo closely resembled the structures of other bacterial RPo. The single-stranded ntDNA could be traced in all three structures. In contrast, the density for the single-stranded tDNA in the RNAP cleft was mostly absent in P-rrna and P-gre RPo without CarD but could be fully traced in P-gre RPo with CarD (**Figure S5**). CarD binds to RNAP in canonical conformation closely resembling the binding mode previously observed in Mycobacteria and Deinococcota [34–36] (**Figure 5A**). Specifically, CarD binds to a protrusion with its N-terminal tudor domain and inserts a conserved Trp of its C-terminal α-helical domain into the minor groove just upstream of the -10 promoter element. The same binding pose was observed at both CarD-stimulated P-rrna and CarD-attenuated P-gre promoters. Overall, spirochetal CarD is well positioned to promote melting of the -10 element, secure the upstream DNA binding to the holoenzyme and indirectly facilitate further steps in promoter melting.

Structure of *S. africana* RPo: lineage-specific inserts

CryoEM reconstructions of *S. africana* RPo revealed the structural fold of major lineage-specific inserts Si1 and Si3 (**Figure 5A**). The structures showed that spirochetal Si1 is a substructure of *E. coli* Si1 and features the same overall fold. Spirochetal Si1 is missing

the subdomain (named Si1-1.2 by Parshin *et al.*) that has been implicated in functioning of *E. coli* DksA [21]. For consistency, we refer to Si1-1.2 as Si1-ni, for nested insertion. *E. coli* DksA influences promoter melting by inserting itself between Si1, Si3 and the Rim Helices (RH), thereby changing the mobility of the β lobe domain that in turn affects the σR1.1 ejection and promoter melting [23]. *E. coli* Si1-ni forms the bulk of the contact interface between DksA and Si1 (**Figure 5B** and PDB ID 7KHI). The absence of Si1-ni in spirochetes may therefore prevent the Si1 from interacting with DksA, effectively decoupling the entire lobe from DksA. Nevertheless, our biochemical data show that *S. africana* DksA strongly affects transcription initiation *in vitro*. Furthermore, two large bacterial superphyla, PVC+ (Planctomycetota, Verrucomicrobiota, Chlamydiota and related phyla) and FCB+ (Fibrobacterota, Chlorobiota, Bacteroidota and related phyla), feature DksA and Si1 without Si1-ni (**Figure 1C-D**). These observations suggest that while *E. coli* DksA evolved to depend on the Si1-ni for functioning, DksA from Spirochaetota, PVC+ and FCB+ utilize rudimentary mechanisms that do not require Si1-ni.

S. africana Si3 has the same overall fold as *E. coli* Si3, with the *E. coli* insert being a substructure of the *S. africana* insert. *S. africana* Si3 incorporates an additional phylum-specific domain that we named Si3-ni, for nested insertion (**Figure 5A-B**, dark green). Si3-ni rests on the β′ Shelf region and is distant from the RH, Jaw, and Si1. Therefore, the presence of Si3-ni does not compensate for the absence of the Si1-ni. *E. coli* Si3 positions the Jaw domain [37,38] to interact with downstream DNA in RPo. Interestingly, although the Jaw domain is present in all bacterial RNAPs, it only interacts with downstream DNA when positioned by the canonical Si3 (e.g. PDB ID 7MKD). In RPo formed by Si3-less RNAPs (e.g. PDB IDs 7KIN, 7CKQ) or those with non-canonical Si3 (e.g. PDB ID 8GZG), the Jaw is completely disengaged from the downstream DNA. Our cryoEM reconstructions revealed that spirochetal Si3 positions the Jaw to interact with downstream DNA in a manner similar to that in *E. coli* RPo thereby reaffirming the trend described above (**Figure 5A**).

Structure of *S. africana* RPo: upstream DNA and σR4

A noticeable unique characteristic of *S. africana* RPo is the α-helical protrusion of the σNCR (σ non-conserved region) that extends towards the β subunit N-terminal zinc binding domain (ZBD) and contacts the phosphate backbone of the template DNA strand at registers -17 to -19 (**Figure 5A-B**). As a result, the σR2-proximal upstream

DNA duplex is almost completely encircled by the proteinaceous environment: tDNA -13 to -15 is contacted by CarD, -17 to -19 by the σNCR protrusion, whereas ntDNA -14 to -17 is contacted by σR2 and σR3. Interestingly, the α-helical protrusion of the σNCR occupies a similar volume to that of the C-terminal region of the transcription factor RbpA in mycobacterial RPo (**Figure 5C**). Thus, some of the RPo stabilizing functionality of mycobacterial RbpA (not present in spirochetes) could be encoded in the spirochetal σ itself in the form of α-helical protrusion of the σNCR.

The main chain atoms of σR4 domains align well in *S. africana* and *E. coli* RPo structures, and the amino acid sidechains implicated in the recognition of the -35 promoter element [39] are conserved (Arg561/584 Glu562/585, Gln566/589; *S. africana* and *E. coli* numbers respectively). However, closer examination of CarD-bound structures revealed that the recognition α-helix of σR4 interacts with the upstream DNA in an atypical and non-sequence-specific manner. σR4 usually interacts with the upstream DNA as a standard helix-turn-helix motif: the N-terminal tip of the recognition α-helix inserts halfway into the major groove and forms base-specific contacts with the -35 promoter element, while the positioning α-helix interacts with the phosphate backbone (**Figure 5C-D**, bottom panels). In *S. africana* RPo, the spacer DNA slightly curves towards the β Flap and β' Dock (**Figure 5C-D**, top panels). This curving causes a significant shift of the upstream DNA duplex from its usual location when it approaches σR4: the entire recognition α-helix of σR4 is inserted into the major groove, potentially interacting with the phosphate backbone but unlikely forming base-specific contacts with the -35 promoter element. Consistently, both the upstream DNA and σR4 are positioned nearly identically in the structures of P-gre and P-rrna RPo featuring 16 bp and 17 bp spacers, respectively, suggesting the absence of sequence-specific contacts between σR4 and the -35 element.

In the CarD-less RPo, the upstream DNA exhibits significant flexibility, allowing for reconstruction of four distinct structural states. Two of these states (II and III) feature the -35 element canonically engaged with σR4, while the other two (I and IV) display disengaged conformations, similar to those observed in CarD-bound RPo at P-gre and P-rrna (**Figure 5C-D**, **Video S2**). Interestingly, the helical protrusion of σNCR appears partially disordered when the -35 element is canonically engaged (states II and III) (**Figure 5C**, bottom right) but fully ordered when the upstream DNA is disengaged (all other structures of *S. africana* RPo). This suggests a connection between the upstream DNA disengagement and the helical protrusion of σNCR.

Structure of *S. africana* holoenzyme dimer bound to DNA

During cryoEM structural analysis of *S. africana* holoenzyme at the P-gre promoter, using high concentrations of holoenzyme and DNA, we unexpectedly observed a complex featuring two holoenzyme protomers interacting with the central DNA duplex in a non-sequence-specific manner (**Figure 6**). Each holoenzyme protomer additionally contains a DNA duplex end-bound in the downstream DNA channel: an *in vitro* artifact due to abundant DNA ends previously observed also in the *E. coli* system (PDB ID 7KHC). **Figure 6A** illustrates the overall mode of holoenzyme engagement with the central DNA duplex, whereas schematic in **Figure 6B** reveals the core architecture of the complex: two holoenzyme protomers dimerize via ZBDs and interact with the central duplex DNA via αCTD and the σR4 recognition helix. The two protomers are related through a 180-degree rotation around an axis that passes through the interface between the ZBDs and is perpendicular to the plane of the page. With the core architecture in mind, it becomes evident from the leftmost image in **Figure 6B** that the space between the protomers is occupied by two interlocked σNCR domains, one from each protomer.

The most interesting feature of the complex is the mode of interaction with the central DNA duplex. The σR4 recognition helix of each protomer clearly engages the minor groove of the straight DNA duplex: an inherently non-sequence-specific type of interaction (**Figure 6C**). Each protomer interacts with the central DNA duplex via a forked arm composed of σR4 and the α2CTD. The forked arm resembles the αCTD dimer interacting with the UP-element at *E. coli* rrnB P1 (PDB ID 7KHC), but the σ recognition helix is involved instead of the α1CTD, and the interaction with DNA takes place much closer to the RNAP body. The forked arms contributed by each protomer interact with the minor groove one helical turn apart (10-11 bp, **Figure 6C**) and are related by a 180 degrees rotational symmetry as do the entire protomers. The same interaction can be principally formed by a monomeric holoenzyme using a single forked arm, albeit with a reduced affinity due to the loss of cooperativity between protomers.

Another interesting feature of the structure is an additional α-helical density observed in the volume bordered by σR2, the σNCR helical protrusion and σR3. In RPo this volume is occupied by the duplex DNA immediately upstream of the -10 element. We attributed this additional density to the σR1.1 globular domain (**Figure 6A**, magenta cartoon). To verify this assignment, we probed the location of σR1.1 in *S. africana*

holoenzyme by *in vitro* crosslinking with disuccinimidyl sulfoxide (DSSO) followed by mass spectrometry analysis (CLMS). We identified two distinct clusters of Lys residues that crosslink to Lys residues within σR1.1 (**Figure S6**). σR1.1-crosslinkable Lys residues in Switch 2 region, the Rudder Loop, and the Jaw domain suggest that σR1.1 is located in the downstream DNA channel, as observed in structures of *E. coli* holoenzyme [40,41] and early intermediates in the promoter melting pathway [23,42]. At the same time, σR1.1-crosslinkable Lys residues in σR2, σR3, σNCR, and CarD suggest that σR1.1 is located in place of the upstream fork junction supporting our assignment of the additional density to σR1.1. Our CLMS analysis suggests that σR1.1 naturally alternates between locations in the downstream DNA channel and near σR3.

S. africana holoenzyme efficiently binds DNA in a non-sequence-specific manner

Given that the dimeric holoenzyme complex with DNA used in structural analysis was assembled at a high concentration of RNAP and DNA, we used an electrophoretic mobility shift assay (EMSA) to investigate the binding of *S. africana* and *E. coli* holoenzymes to DNA at physiologically relevant concentrations. The promoter DNA fragment contained the P-gre promoter, 28 bp of DNA downstream of the TSS, and 101 bp of DNA upstream of the -35 element (**Figure 6E**). Addition of 4 μM of *S. africana* σ to 25 nM of the promoter DNA fragment resulted in a distinct, slower-migrating band, that we interpreted as a σ-DNA complex. Subsequent addition of 25 nM RNAP led to an even slower-migrating band, that we interpreted as a promoter-bound holoenzyme-DNA complex (holo-DNA). This interpretation was supported by the formation of a similarly sized band when the DNA fragment was titrated with *E. coli* holoenzyme. Increasing *S. africana* RNAP concentration to 100 nM caused the disappearance of σ-DNA and holo-DNA bands and the emergence of an even slower-migrating band, which we termed the multi-holoenzyme-DNA complex ($holo_n$-DNA). This complex likely consists of a promoter-bound holoenzyme and additional holoenzyme(s) bound non-specifically upstream. In contrast, we did not observe formation of multi-holoenzyme-DNA complexes when titrating with *E. coli* holoenzyme. We also titrated a promoter-less DNA fragment with *S. africana* and *E. coli* holoenzymes and observed formation of distinct complexes in the former but not the latter case (**Figure 6E**). These findings indicate that the *S. africana* but not *E. coli* holoenzyme possesses a strong tendency for non-sequence-specific association with DNA at physiological concentrations.

Discussion

We report a comprehensive structural-functional analysis of transcription initiation in Spirochaetota. This diderm bacterial phylum is the most basal lineage within the Pseudomonadati kingdom and is markedly divergent from characterized model systems. We show that spirochetal transcription initiation displays a combination of features from both *E. coli* and Mycobacteria. Structurally, the spirochetal RPo is similar to that of *E. coli* and less so to Mycobacteria and Bacilli, consistent with sequence and phylogenetic analyses. In particular, spirochetes feature lineage-specific sequence inserts Si1 and Si3 that have been implicated in stabilizing RPo and regulation of transcription initiation by DksA in *E. coli*. However, biochemically, the spirochetal holoenzyme behaves more like the mycobacterial enzyme, exhibiting a weaker intrinsic ability to melt promoter DNA. This deficiency is overcome by the CarD activator, which is structurally similar to its mycobacterial counterpart and functions analogously in spirochetes. This differs from the situation in α-proteobacteria, where CarD has a more specialized function and primarily facilitates melting of promoters with non-canonical -10 elements [43].

In contrast to mycobacteria, spirochetes possess a DksA regulator, similar to that found in *E. coli*. We demonstrate that *S. africana* DksA functions as a pH-responsive negative regulator of ribosomal RNA transcription but suggest that its overall regulatory repertoire might be reduced due to spirochetes lacking the Si1-ni subdomain that is important for the full functionality of *E. coli* DksA [21]. In particular, inhibition of *S. africana* holoenzyme by DksA was not enhanced by ppGpp, which contrasts with the strong DksA-ppGpp synergy observed in the *E. coli* system. These results align with *in vivo* studies in *Borrelia*. Although ΔDksA *Borrelia* strains show deficiencies in adapting to nutrient-limited conditions, reduced virulence, and altered transcriptomes [44–46], DksA and ppGpp regulation appear to function independently, in parallel.

Resistance to rifampicin is a unique and conserved feature of spirochetal RNAPs, the functional significance of which remains unclear given that these species inhabit various environments and are not universally exposed to rifampicin-like compounds. In other bacterial phyla, acquiring rifampicin resistance often incurs a fitness cost [47,48]. However, the rifampicin-sensitive βN490S RNAP displayed the same activity at spirochetal promoters as the wild-type *S. africana* RNAP. A converse βS351N change in the *E. coli* RNAP also did not affect its performance at spirochetal promoters. Interestingly,

βS351N significantly reduced activity of *E. coli* RNAP at *E. coli*'s own rrnB P1, whereas *S. africana* holoenzymes exhibited very low activity at rrnB P1, both with and without CarD (**Figure 4C-D**). These observations are consistent with the idea that spirochetes may utilize a limited set of promoters where rifampicin resistance does not impose a fitness cost, in contrast to *E. coli*'s broader range of promoters.

Our structural analysis revealed that the spirochetal holoenzyme disengages the -35 promoter element from σR4 upon promoter melting. This contrasts with other bacterial holoenzymes studied to date, which maintain interactions with both the -35 and -10 promoter elements during RPo formation. Recent structural studies of deinococcotal and mycobacterial RNAPs showed that -35 disengagement occurs late during the initial transcription via the allosteric displacement of the σ-finger (a loop region linking σR3 and σR4) by the extending RNA-DNA hybrid (**Figure 7A**) [49,50]. Notably, -35 disengagement precedes, and may be essential for the subsequent release of the -10 element in the mycobacterial system. In the spirochetal system, the coupling of -35 disengagement with promoter melting may facilitate the earlier release of the -10 promoter element during the initial transcription, leading to a promoter escape pathway with less DNA scrunching compared to other bacterial systems (**Figure 7A**). This may contribute to the efficient initiation at consensus-like promoters such as P-gre and P-pori, where *S. africana* RNAP outperforms the *E. coli* counterpart.

The spirochetal holoenzyme displays an unusually strong, non-sequence-specific association with DNA and can bind to the minor groove (**Figure 6**). Collectively, these findings suggest that the spirochetal holoenzyme predominantly exists in a DNA-associated form and navigates the genome via one-dimensional facilitated diffusion mechanisms, such as sliding and hopping (**Figure 7B**). This contrasts with the *E. coli* holoenzyme, which primarily explores the genome through three-dimensional diffusion [51,52]. This difference may be functionally related to the distinct cellular morphologies: *E. coli* cell is a 0.5 × 1-3 μm rod with a compact nucleoid, while *S. africana* is 0.25-0.3 μm thick and 15-30 μm long [26]. Given that the spirochetal nucleoid stretches along the entire length of the bacterium [53], such a highly anisotropic environment may render three-dimensional diffusion inefficient, necessitating one-dimensional facilitated diffusion for efficient genome exploration.

Our study of the spirochetal transcriptional apparatus reveals significant phylum-level functional diversity of RNAPs within the Pseudomonadati kingdom. These findings

underscore the importance of thorough biochemical and structural characterization of diverse RNAPs and lay the foundation for understanding transcription regulation in pathogenic spirochetes such as *Treponema*, *Borrelia*, and *Leptospira*.

Data availability

CryoEM reconstructions have been deposited in the Electron Microscopy Data Bank (https://www.ebi.ac.uk/pdbe/emdb) under accession codes: 56405, 56406, 56407, 56408 for monomeric RPo-P-gre (state I to IV), 56409 for dimeric RPo-P-gre, 56410 for CarD-RPo-P-gre as well as 56411 for CarD-RPo-P-rrna.

Structure coordinates have been deposited in the RCSB Protein Data Bank (https://www.rcsb.org) under accession codes: 9TXX, 9TXY, 9TXZ, 9TX0 for monomeric RPo-P-gre (state I to IV), 9TX1 for dimeric RPo-P-gre, 9TX2 for CarD-RPo-P-gre as well as 9TX3 for CarD-RPo-P-rrna.

RNA-seq data have been deposited in the GEO database (https://www.ncbi.nlm.nih.gov/geo/query/acc.cgi?acc=GSE305863)

All other data are contained in the manuscript or the Supplementary Information. Supplementary Data File is provided in this paper.

This paper does not report original code. Any additional information required to reanalyze the data reported in this paper is available from the lead contact upon request.

Acknowledgements

Work in the authors' laboratories was supported by grants from the Academy of Finland (341962 to G.A.B.), the Sigrid Jusélius Foundation (to G.A.B.) and the Deutsche Forschungsgemeinschaft (WA 1126/11-1 to M.C.W.). We thank Irina Artsimovitch, Ohio State University, for critically reading the manuscript. We acknowledge the assistance of the Core Facility BioSupraMol supported by the German Research Foundation (Deutsche Forschungsgemeinschaft). We are grateful to Jörg Bürger, Freie Universität Berlin, Research Center of Electron Microscopy and Core Facility BioSupraMol, for help with cryoEM sample preparation. The study utilized protein expression and purification infrastructure provided by Turku Protein Core. Transcriptome sequencing was performed by the Finnish Functional Genomics Centre, the University of Turku and

Åbo Akademi, supported by the Biocenter Finland. The authors wish to acknowledge CSC – IT Center for Science, Finland, for computational resources. Mass spectrometry analyses were performed at the Turku Proteomics Facility supported by Biocenter Finland. We thank Verneri Nissilä, Iida Payne, Oskari Puro and Karina Šapovalovaitė for their assistance with assay development and experimental condition screening during the initial phases of this study.

Author contributions

V.K.T. most FLAP assays, RNA isolation from spirochetes. T.W. cryoEM analyses, sample preparation, model building. T.H. cryoEM analyses and data processing. J.J.M. reconstitution of spirochetal transcription *in vitro*. J.K. nanopore sequencing, transcriptome analysis. P.J.T. EMSA experiments. V.L. FLAP assays. B.L. cryoEM analyses, model building and refinement. Protein production: T.W., J.J.M., S.P., V.K.T., V.L., J.K. Plasmids construction: T.W., J.J.M., V.L., J.K. Large scale DNA production: V.L., J.K., V.K.T. Crosslinking mass-spectrometry: V.K.T, S.P., J.J.M. Cultivation of spirochetes: V.K.T, S.P., J.K. All authors contributed to the analysis of the data and the interpretation of the results. M.C.W. and G.A.B. conceived, designed, supervised the study and wrote the manuscript with contributions from the other authors.

Declaration of Interests

The authors declare no conflict of interest.

Declaration of AI-assisted technologies in the writing process

The authors used Gemini AI to improve language and readability. The author reviewed and edited AI suggestions and takes full responsibility for the final content of the document.

Methods

Reagents

NTPs from Jena Bioscience, Bioline Reagents and Thermofisher were used interchangeably in *in vitro* transcription assays. DFHBI-1T (CAS Number: 1539318-36-9) was from Jena Bioscience and TargetMol. Other reagents were purchased from Merck and Fisher Scientific.

Molecular phylogenetic analysis

Protein sequences of RNAP β, β′, α subunits and NusA transcription elongation factor were fetched from the KEGG database [54]. 2-5 divergent sequences per phylum were selected (**Table S1**) to achieve balanced representation of different bacterial phyla. Protein sequences were concatenated, aligned with Muscle (default settings) [55] and conserved blocks of sequences were extracted using Gblocks (default settings) [56]. A molecular phylogenetic tree was constructed using MrBayes software [57] using the empirical Jones-Taylor-Thornton amino acid substitution matrix[58], the rate heterogeneity across sites was modeled with 8 gamma categories [59]. The analysis was run for 200,000 generations, trees were sampled every 1,000 generations, the first 50 trees (50,000 generations) were discarded, and the consensus tree was built from the remaining 150 trees. Seaview [60] and Ugene [61] software packages were used as graphical user interfaces to run Muscle, Gblocks, MrBayes and visualize molecular phylogenetic trees. For indel analysis, the correspondence (likely homology) between positionally aligned lineage-specific inserts (Si1, Si2 and Si3) was estimated based on experimentally determined structures (where available) or AlphaFold [62] models of individual RNAP subunits (precomputed [63] or generated using the AlphaFold Server (https://alphafoldserver.com/) [64]).

Plasmids for protein expression in *E. coli*

Plasmids employed for protein expression are presented in **Table S3**. Wild-type and variant *S. africana* and *E. coli* RNAPs were produced from polycistronic vectors encoding αββ′ω subunits with polyhistidine tags at the C-terminus of β′, the N-terminus of β or both. Wild-type and variant *S. africana* σ factors, CarD, DksA, *E. coli* σ factor and DksA were produced from plasmids encoding gene fusions with N-terminal polyhistidine tags followed by a TEV, ULP1 (SUMO domain) or thrombin protease site.

Plasmids used as transcription templates

All transcription template plasmids (**Table S4**) were derivatives of pOP004 and contained the identical ~2.4 kb pOA-RQ backbone (containing the ColE1 origin and encoding β-lactamase) and a ~1 kb insert between *Sfi*I sites. The insert contained a transcription unit consisting of a promoter and a 0.8 kb transcribed region ending with a strong hairpin-dependent terminator. The transcribed region encoded a Broccoli fluorogenic light up aptamer [65] embedded in a tRNA scaffold just upstream of the terminator. The upstream 0.2 kb of the insert was unique for each plasmid and

contained an *Xba*I-*Nhe*I module encompassing a promoter with flanking genomic sequences (40 bp upstream of the -35 element and 20 bp downstream of the transcription start site). The downstream 0.8 kb of the insert were the same for all plasmids except for pJK006 and pJK004 contained a featureless *Nhe*I-*Mfe*I module, a *Mfe*I-*BsrG*I module encoding a Broccoli aptamer, followed by a *BsrG*I-*Xho*I module encoding the *E. coli hisT* terminator. In the pJK006 and pJK004 plasmids, phage λ Rho utilization sites were inserted near the upstream edge of the *Nhe*I-*Mfe*I module. Plasmids stocks (1-2 μM) were produced from 0.5-1 l of LB culture using NucleoBond Xtra Maxi kit (Macherey-Nagel). 500 nM stocks of linearized plasmids were prepared by digestion with *Xho*I restriction enzyme in the Thermofisher Buffer R (10mM Tris-HCl pH 8.5 at 37°C, 10 mM $MgCl_2$, 100 mM KCl, 0.1 mg/ml BSA) and used directly in *in vitro* transcription assays.

Protein production in *E. coli*

Individual components of *S. africana* and *E. coli* transcription systems were expressed in *E. coli. E. coli* Xjb(DE3), BL21(DE3) and T7 Express lysY/Iq (New England Biolabs) stains were used interchangeably unless indicated otherwise. Cultivation was performed in 4 l of LB medium in flasks or a fermenter. Cells were harvested by centrifugation at 7,000 × g for 20 min at 4°C. Cultivations yielded from 15 g (5 h induction) to 20-40 g (overnight induction) of cells. *E. coli* proteins were produced using 5 h induction with IPTG at 30°C. *S. africana* proteins other than σ factors were produced using the overnight express autoinduction protocol [66] at 37°C (≥18 h). *S. africana* σ factor was produced in *E. coli* T7 Express *lys*Y/I^q cells. Cells were pre-grown to OD_{600} 0.6 and induced with 1 mM IPTG overnight at 25°C.

Purification of proteins produced in *E. coli*

Wild-type and variant RNAPs and σ factors were purified by combination of Ni^{2+}-affinity, heparin and anion exchange chromatography [67]. Cells (20-40 g) were resuspended in Lysis Buffer (50 mM Tris-HCl pH 7.9, 5% (v/v) glycerol, 500 mM NaCl, 1 mM β-mercaptoethanol) supplemented with EDTA-free protease inhibitor cocktail (Pierce or Roche). At least 30 ml of lysis buffer was used per 5 g of cells. When using *E. coli* BL21(DE3) or T7 Express lysY/Iq cells, the lysis buffer was supplemented with 1 mg/ml of lysozyme and the cells were incubated on ice for 1 h prior to disruption by sonication, whereas *E. coli* Xjb(DE3) cells were disrupted immediately following the resuspension in lysis buffer without lysozyme. Lysates were clarified by centrifugation

at 40,000 × g for 30 min at 4°C. Clarified lysates were loaded onto 3 gravity columns each containing 1 ml of WorkBeads NiMAC (Bio-Works) chromatography matrix. Columns were washed with 10 ml of lysis buffer, and the target protein was eluted with a step gradient of imidazole (50, 100 and 200 mM, 10 ml each passed sequentially through the 3 columns) in Lysis Buffer. Fractions containing the target proteins were diluted three times with buffer A (50 mM Tris-HCl pH 7.9, 5% (v/v) glycerol, 1 mM β-mercaptoethanol, 0.1 mM EDTA) and loaded onto a 5 ml heparin column (HiTrap® Heparin HP, Cytiva) equilibrated with 10% buffer B (50 mM Tris-HCl pH 7.9, 1.5 M NaCl, 5% (v/v) glycerol, 1 mM β-mercaptoethanol, 0.1 mM EDTA), washed with 15-30 ml of 10% buffer B, and the target protein was eluted with a 100 ml gradient of buffer B (10-100%). Fractions containing the target protein were pooled, diluted 2-3 times with buffer A and loaded onto a 6 ml ResourceQ column (Cytiva) equilibrated with 10% buffer B, washed with 15-30 ml of 10% buffer B, and the target protein was eluted with a 100 ml gradient of buffer B (10-100%). Fractions containing the target protein were pooled, concentrated using ultrafiltration concentrators, dialyzed against storage buffer (50% (v/v) glycerol, 20 mM Tris-HCl pH 7.9, 150 mM NaCl, 0.1 mM EDTA, 0.1 mM DTT) and stored at -20°C (short term) or -80°C (long term). For target proteins with cleavable N-terminal polyhistidine tag, removal of the tag was performed either after elution from WorkBeads NiMAC or after heparin chromatography by overnight digestion with in-house produced TEV (His_6-TEV-gene constructs) or in-house produced ULP1 protease (His_6-SUMO-gene constructs). Prior to digestion with proteases, the NaCl concentration was reduced to 0.3 M by dilution with buffer A. *S. africana* CarD, DksA and *E. coli* DksA were purified using capture on WorkBeads NiMAC as described above followed by cleavage of the polyhistidine tag and size exclusion chromatography on a 120 ml HiPrep™ Sephacryl™ S-200 HR 16/60 column (Cytiva) in 33 or 50% buffer B.

Production of *Sfc* RNAP *via* recombinant baculovirus in insect cells

Plasmid pFL-AC_pUCDM-BZ was created from the donor plasmid pUCDM (with *S. africana rpoB* and *rpoZ* genes encoding β and ω subunits, respectively) and the acceptor plasmid pFL (with *S. africana rpoA* and *rpoC* genes encoding α and β′ subunits, with β′ fused to a C-terminal His_6-tag) *via* Cre-LoxP recombination [68]. The resulting pFL-AC_pUCDM-BZ plasmid was introduced into DH10MultiBac *E. coli* cells to produce recombinant bacmid. The bacmid was transfected into Sf9 cells to produce generations V1 and V2 of recombinant baculovirus particles. 400 ml Hi5 cell culture at 0.8 x 10^6

cells/ml were infected with 1 ml V2 virus. Cells were further cultured at 27 °C with shaking (80 rpm), split after 24 h and, after an additional 48 h incubation, harvested by centrifugation.

All purification steps were conducted at 4 °C. The cell pellet was resuspended in 40 ml lysis buffer (50 mM Tris-HCl, pH 6.9, 500 mM NaCl, 5 % (v/v) glycerol), supplemented with cOmplete™ EDTA-free protease inhibitor (Sigma-Aldrich), 1 mg/ml DNase, 1 mM β-mercaptoethanol and 0.2 % (v/v) Tween 20, and disrupted by sonication. The lysate was cleared by centrifugation, and the supernatant was loaded onto a Ni^{2+}-NTA HisTrap column (Cytiva) pre-equilibrated with lysis buffer. Proteins were eluted using a linear gradient (20 - 250 mM) of imidazole in lysis buffer. Fractions containing *S. africana* RNAP were identified by SDS PAGE, pooled and diluted 1:4 with buffer A (50 mM Tris-HCl, pH 6.9, 5 % (v/v) glycerol, 1 mM β-mercaptoethanol, 0.1 mM EDTA). *S. africana* RNAP was further purified using HiTrap Heparin HP and HiTrap MonoQ HP columns (Cytiva) with analogous dilution in between and using gradients to buffer A plus 1.5 M NaCl. Fractions containing *S. africana* RNAP were pooled, and the target was further purified by size exclusion chromatography (SEC) on a HiLoad Superdex 200 Increase 16/600 column (Cytiva) in storage buffer (50 mM Tris-HCl, pH 6.9, 300 mM NaCl, 0.1 mM EDTA, 2 mM DTT, 10 % (v/v) glycerol). Fractions containing *S. africana* RNAP were concentrated to approximately 8 mg/ml, aliquoted, flash-frozen in liquid nitrogen, and stored at -70 °C.

S. africana σ^{70} holoenzyme was prepared by mixing 10 μM (yielding monomeric complexes) or 20 μM (yielding dimeric complexes) RNAP with a threefold molar excess of σ^{70} and incubation for 10 min at 32 °C. Template (tDNA) and non-template DNA (ntDNA) were mixed at equimolar concentrations in binding buffer (20 mM Tris-HCl, pH 7.9, 120 mM KOAc, 5 mM $Mg(OAc)_2$, 10 μM $ZnCl_2$, 2 mM DTT) and annealed by heating to 95 °C for 5 min and subsequent cooling to 25 °C at 1 °C/min. The annealed scaffolds were incubated with *S. africana* σ^{70} holoenzyme in a 1.3:1 molar ratio for 10 min on ice, followed by an additional incubation for 10 min at 32 °C. The mixture was subjected to SEC on a Superdex 200 Increase 3.2/300 column in binding buffer. Fractions containing *S. africana* σ^{70} promoter complexes were identified by SDS PAGE and urea PAGE analysis, pooled and concentrated to 5-6 mg/ml by using a 100 kDa cutoff Amicon Ultra Centrifugal Filter (Sigma-Aldrich).

S. africana CarD-modified σ^{70} promoter complexes were prepared by mixing 20 μM RNAP with σ^{70} and, subsequently, CarD, each at threefold molar excess, with incubation for 10 min at 32 °C after each step. Equimolar tDNA and ntDNA were annealed as above, mixed with *S. africana* CarD/holoenzyme mix in a 1.3:1 molar ratio and incubated for 10 min on ice, followed by incubation for 10 min at 32 °C. The mixture was subjected to SEC in binding buffer as above. Fractions containing CarD-modified σ^{70} promoter complexes were pooled and concentrated to 5-6 mg/ml as above.

Fluorogenic light-up aptamer *in vitro* transcription assays

FLAP assays were performed largely as described previously [28]. Reactions were initiated by mixing 35 μl of holoenzyme-DNA solution with 35 μl of NTP solution. Both solutions contained the transcription buffer and were pre-warmed at 37°C. Within 20 s, 55 μl of the reaction mix was transferred to the ultra-micro fluorometer cuvette (Hellma 105.251-QS) pre-warmed at 37°C, the cuvette was placed in the fluorometer equipped with a thermostated cuvette holder at 37°C, and fluorescence was recorded in a time-drive mode for 10 min. The reaction mixture contained 10 μM of (5Z)-5-[(3,5-difluoro-4-hydroxyphenyl)methylene]-3,5-dihydro-2-methyl-3-(2,2,2-trifluoroethyl)-4H-imidazol-4-one (DFHBI-1T), 1 mM each of ATP, CTP, GTP and UTP, 50 nM of linearized plasmid DNA template, 100 nM yeast inorganic pyrophosphatase, 1 μM RNAP, 4 μM σ. Transcription buffers contributed 10 mM $MgCl_2$, 80 mM KCl, 0.1 mM EDTA, 0.1 mM DTT and 40 mM of zwitterionic buffer (HEPBS-KOH pH 9.0, HEPBS-KOH pH 8.5, HEPPS-KOH pH 8.0, HEPES-KOH pH 7.5; all pH values at 25°C) to the reaction mixture. Taking into account the contributions of the storage buffer (from proteins), buffer R (from DNA templates) and NTPs (disodium salts), the final reaction mixture contained 11 mM $MgCl_2$, 110-120 mM KCl, 25 mM NaCl, 3 mM Tris, 5% (v/v) glycerol, 1% (v/v) DMSO, and 0.01 mg/ml BSA.

Fluorescence time curves were highly reproducible within the single experiment and across independent experiments performed days apart with the same batch of RNAP. However, the absolute activities of different batches of RNAP differed by as much as twofold and decreased upon storage on the timescale of weeks. All major effects reported in this study were confirmed by the direct comparison within the same experiment. The reported absolute activities were adjusted based on activity of the P-gre promoter that was measured in each experiment. A median activity of the P-gre promoter with fresh batches of RNAP was used as a reference.

In a subset of experiments, we employed an end-point-only modification of the FLAP assay to facilitate rapid acquisition of data. Reactions were initiated by mixing 20 μl of holoenzyme-DNA solution with 20 μl of NTP solution. Both solutions were pre-warmed at 37°C and did not contain DFHBI-1T and 1% DMSO. The reactions were incubated for 10 min in a thermoblock at 37°C and quenched by 20 μl of solution containing 45 mM EDTA (15 mM final) and 30 μM DFHBI-1T (10 μM final). For zero samples, holoenzyme-DNA solution was mixed with quench solution before adding NTP solution. 55 μl of the quenched reaction mix were transferred to the fluorometer cuvette, the cuvette was placed in the fluorometer equipped with a thermostated cuvette holder at 25°C, and the fluorescence spectrum was recorded (490-600 nm, excitation at 472 nm). Fluorescence at 507 nm corrected for the fluorescence of the zero samples and multiplied by 1.5 to account for the dilution during quenching was then used as a measure of transcription activity.

Denaturing PAGE analysis of RNA products

Transcription reactions were set up as described in the FLAP assay section. A 20 μl aliquot was withdrawn after 10 min and quenched by 60 μl of Gel Loading Buffer (94% formamide, 20 mM Li_4-EDTA and 0.2% OrangeG). RNAs (1.5 μl) were separated on 6% 10 × 12 cm denaturing TBE-urea polyacrylamide gels (30 min at 70 V followed by 75 min at 180 V) in 1×TBE buffer, stained with SYBR-Gold for 30 min in 1×TBE buffer, and visualized with a Sapphire FL Biomolecular Imager (Azure Biosystems). Gel images were processed using the ImageJ software [69].

Analysis of RNA products using Qubit fluorometer

Transcription reactions (70 μl, in order to use the same pipetting volumes as in the FLAP assays) were set up as described in the FLAP assay section except that DFHBI-1T was omitted. Reactions were quenched after 10 min by withdrawing a 40 μl aliquot and mixing it with 10 μl of 0.5 M EDTA (100 mM final). For zero samples, EDTA was added to the holoenzyme-DNA solution before mixing with the NTP solution. 2-20 μl of quenched reactions were mixed with Qubit Broad Range RNA assay reagent (Thermofisher) to achieve the final volume of 200 μl. The apparent RNA concentration was then determined by measuring the sample fluorescence using the Qubit instrument (version 4, Thermofisher) calibrated using RNA standards. The actual RNA concentration in the sample was then estimated by subtracting the zero sample readings (~25 nM).

CryoEM grid preparation, data acquisition and processing

Samples were supplemented with 0.15 % (w/v) n-octylglucoside. A 3.8 µl aliquot of the sample was applied to glow-discharged Quantifoil R 1.2/1.3 Cu grids at 10 °C and 100 % humidity, and blotted using a FEI Vitrobot Mark IV with a blot force setting of -10, a waiting time of 4 s and a blotting time of 4 s. The grids were then plunged into liquid ethane, cooled by liquid nitrogen, and stored in liquid nitrogen until data collection.

Images were collected at a nominal magnification of 96,000x in counting mode, using a FEI Titan Krios G3i transmission electron microscope (TEM) at 300 kV, equipped with a Falcon 3EC camera, using the EPU software (ThermoFisher Scientific) with a calibrated pixel size of 0.832 Å. A total electron dose of 40 $e^-/Å^2$ was accumulated over an exposure time of 40.57 s. Movie alignment was done with Patch Motion correction, followed by contrast transfer function (CTF) estimation with PatchCTF within cryoSPARC [70].

For cryoEM image processing, all steps were performed using cryoSPARC [70]. For monomeric *S. africana* σ^{70} promoter complexes, 6,990 micrographs were collected (**Figure S7**). Micrographs showing defects in the Thon rings due to excessive drift, ice contamination or astigmatism were discarded. An initial model for reference-based particle selection from micrographs was created using class averaging of manually selected particles. In the initial analysis, particle images were extracted by using a box size of 440, binned to 110. All raw particles were automatically selected and submitted for 2D classification to remove poor-quality particles. After 2D classification, 1,925,988 particles were retained for further analysis. *Ab initio* reconstruction was conducted to generate an initial 3D reference for 3D heterogeneous refinement, using a small subset of particles. The dataset was iteratively classified into three populations, and two bad populations were discarded. Selected particles were re-extracted from the good population (849,917 particles) with a box of 220 and 3D classified again to clean the dataset further. Finally, selected particle images were re-extracted with a box of 280 (1.3 Å/px) and subjected to local refinement using a generously enlarged soft-mask. After per-particle CTF correction, non-uniform refinement [71] was applied to generate the final cryoEM maps with an estimated average resolution of 3.0-3.4 Å according to the gold-standard Fourier shell correlation cutoff of 0.143 [72] (**Figs. S7-8**). CryoEM images of dimeric *S. africana* σ^{70} promoter complexes (**Figs. S9-10**) and of CarD-modified σ^{70} promoter complexes (**Figs. S11-12**) were processed in an analogous fashion.

Model building, refinement and analysis

AlphaFold3 models [64] of the individual proteins were computed and manually placed into the cryoEM reconstructions, adjusted by rigid body fitting and segmental real-space refinement using Coot (version 1.11.1) [73,74]. The structural models were refined by iterative rounds of real space refinement in PHENIX (version 1.21.2-5419) [75,76] and manual adjustment in Coot. The structural models were evaluated with MolProbity (version 4.5.1) [77]. Structure figures were prepared with PyMOL (version 2.4.0, Schrödinger) and ChimeraX [78].

EMSA assays

DNA fragments were produced by preparative PCR (0.5-1 ml total volume). Plasmid pVN001, DY782-GGAGAGACAACTTAAAGAGACATTCTG and DY682-TCGTAGATTGTTATTCAACT primers were used to prepare a 163 bp DNA fragment with the P-gre promoter:
GGAGAGACAACTTAAAGAGACATTCTGCATCATGATATTGTTATTATGCTTCCTGC
GGCATATACCCTGCCCATTCTGTGCGCATACCATCCCTGCCTGCGTTGACGAAAC
TCGTTAACATGTTATAATACAAGCGTTACCATAGTTGAATAACAATCTACGA.
Plasmid pVL026, DY782-GGAGAGACAACTTAAAGAGACATTCTG and DY682-TCCTCTGGTTCCTCGTGTCC primers were used to prepare a 163 bp promoter-less DNA fragment:
GGAGAGACAACTTAAAGAGACATTCTGCATCATGATATTGTTATTATGCTTCCTGC
GGCATATACCCTGCCCATTCTGTGCGCATACCATCCCTGCCTGCGCTGCAGGCAC
TGTTTACCGCAGTGCTGCACAAGCATCGAGAGGGACACGAGGAACCAGAGGA.
DNA fragments were purified using the NucleoSpin Gel and PCR Clean-up kit (Macherey-Nagel GmbH). Reactions were prepared by mixing 1 µl of RNAP and 1 µl of σ in storage buffer with 8 µl of DNA fragment in 1.25 × reaction buffer, resulting in 10 µl samples containing 25 nM of DNA fragment, desired concentrations of RNAP and σ, 40 mM HEPBS-KOH pH 9.0, 80 mM KCl, 15% glycerol, 0.1 mM EDTA and 0.1 mM DTT. Reactions were incubated for 20 min at 30°C, mixed with 10 µl of loading solution (20% glycerol and 0.4% OrangeG), and 2 µl was loaded onto a 4% 10 × 12 cm 1×TBE polyacrylamide gel. Electrophoresis was performed for 35 min at 50 V, followed by 25 min at 100 V. DNA bands were visualized with an Odyssey Infrared Imager using 700 nm channel (Li-Cor Biosciences). Gel images were processed using the ImageJ software [69].

References

1. Werner, F., and Grohmann, D. (2011). Evolution of multisubunit RNA polymerases in the three domains of life. Nat. Rev. Microbiol. *9*, 85–98. 10.1038/nrmicro2507.

2. Feklístov, A., Sharon, B.D., Darst, S.A., and Gross, C.A. (2014). Bacterial sigma factors: a historical, structural, and genomic perspective. Annu. Rev. Microbiol. *68*, 357–376. 10.1146/annurev-micro-092412-155737.

3. Chen, J., Boyaci, H., and Campbell, E.A. (2021). Diverse and unified mechanisms of transcription initiation in bacteria. Nat. Rev. Microbiol. *19*, 95–109. 10.1038/s41579-020-00450-2.

4. Lee, D.J., Minchin, S.D., and Busby, S.J.W. (2012). Activating transcription in bacteria. Annu. Rev. Microbiol. *66*, 125–152. 10.1146/annurev-micro-092611-150012.

5. Busby, S.J.W. (2019). Transcription activation in bacteria: ancient and modern. Microbiology (Reading, Engl) *165*, 386–395. 10.1099/mic.0.000783.

6. Rutherford, S.T., Villers, C.L., Lee, J.-H., Ross, W., and Gourse, R.L. (2009). Allosteric control of Escherichia coli rRNA promoter complexes by DksA. Genes Dev. *23*, 236–248. 10.1101/gad.1745409.

7. Paul, B.J., Berkmen, M.B., and Gourse, R.L. (2005). DksA potentiates direct activation of amino acid promoters by ppGpp. Proc Natl Acad Sci USA *102*, 7823–7828. 10.1073/pnas.0501170102.

8. Whipple, F.W., and Sonenshein, A.L. (1992). Mechanism of initiation of transcription by Bacillus subtilis RNA polymerase at several promoters. J. Mol. Biol. *223*, 399–414. 10.1016/0022-2836(92)90660-c.

9. Rojo, F., Nuez, B., Mencía, M., and Salas, M. (1993). The main early and late promoters of Bacillus subtilis phage phi 29 form unstable open complexes with sigma A-RNA polymerase that are stabilized by DNA supercoiling. Nucleic Acids Res. *21*, 935–940. 10.1093/nar/21.4.935.

10. Davis, E., Chen, J., Leon, K., Darst, S.A., and Campbell, E.A. (2015). Mycobacterial RNA polymerase forms unstable open promoter complexes that are stabilized by CarD. Nucleic Acids Res. *43*, 433–445. 10.1093/nar/gku1231.

11. Rammohan, J., Ruiz Manzano, A., Garner, A.L., Stallings, C.L., and Galburt, E.A. (2015). CarD stabilizes mycobacterial open complexes via a two-tiered kinetic mechanism. Nucleic Acids Res. *43*, 3272–3285. 10.1093/nar/gkv078.

12. Zhu, D.X., and Stallings, C.L. (2023). Transcription regulation by CarD in mycobacteria is guided by basal promoter kinetics. J. Biol. Chem. *299*, 104724. 10.1016/j.jbc.2023.104724.

13. Hubin, E.A., Fay, A., Xu, C., Bean, J.M., Saecker, R.M., Glickman, M.S., Darst, S.A., and Campbell, E.A. (2017). Structure and function of the mycobacterial transcription initiation complex with the essential regulator RbpA. eLife *6*, e22520. 10.7554/eLife.22520.

14. Rammohan, J., Ruiz Manzano, A., Garner, A.L., Prusa, J., Stallings, C.L., and Galburt, E.A. (2016). Cooperative stabilization of Mycobacterium tuberculosis rrnAP3 promoter open complexes by RbpA and CarD. Nucleic Acids Res. *44*, 7304–7313. 10.1093/nar/gkw577.

15. Hubin, E.A., Tabib-Salazar, A., Humphrey, L.J., Flack, J.E., Olinares, P.D.B., Darst, S.A., Campbell, E.A., and Paget, M.S. (2015). Structural, functional, and genetic analyses of the actinobacterial transcription factor RbpA. Proc Natl Acad Sci USA *112*, 7171–7176. 10.1073/pnas.1504942112.

16. Danson, A.E., Jovanovic, M., Buck, M., and Zhang, X. (2019). Mechanisms of σ54-Dependent Transcription Initiation and Regulation. J. Mol. Biol. *431*, 3960–3974. 10.1016/j.jmb.2019.04.022.

17. He, D., You, L., Wu, X., Shi, J., Wen, A., Yan, Z., Mu, W., Fang, C., Feng, Y., and Zhang, Y. (2022). Pseudomonas aeruginosa SutA wedges RNAP lobe domain open to facilitate promoter DNA unwinding. Nat. Commun. *13*, 4204. 10.1038/s41467-022-31871-7.

18. Artsimovitch, I., Svetlov, V., Anthony, L., Burgess, R.R., and Landick, R. (2000). RNA polymerases from Bacillus subtilis and Escherichia coli differ in recognition of regulatory signals in vitro. J. Bacteriol. *182*, 6027–6035. 10.1128/JB.182.21.6027-6035.2000.

19. Artsimovitch, I., Svetlov, V., Murakami, K.S., and Landick, R. (2003). Co-overexpression of Escherichia coli RNA polymerase subunits allows isolation and analysis of mutant enzymes lacking lineage-specific sequence insertions. J. Biol. Chem. *278*, 12344–12355. 10.1074/jbc.M211214200.

20. Furman, R., Tsodikov, O.V., Wolf, Y.I., and Artsimovitch, I. (2013). An insertion in the catalytic trigger loop gates the secondary channel of RNA polymerase. J. Mol. Biol. *425*, 82–93. 10.1016/j.jmb.2012.11.008.

21. Parshin, A., Shiver, A.L., Lee, J., Ozerova, M., Schneidman-Duhovny, D., Gross, C.A., and Borukhov, S. (2015). DksA regulates RNA polymerase in Escherichia coli through a network of interactions in the secondary channel that includes Sequence Insertion 1. Proc Natl Acad Sci USA *112*, E6862-71. 10.1073/pnas.1521365112.

22. Shiver, A.L., Osadnik, H., Peters, J.M., Mooney, R.A., Wu, P.I., Henry, K.K., Braberg, H., Krogan, N.J., Hu, J.C., Landick, R., et al. (2021). Chemical-genetic interrogation of RNA polymerase mutants reveals structure-function relationships and physiological tradeoffs. Mol. Cell *81*, 2201-2215.e9. 10.1016/j.molcel.2021.04.027.

23. Shin, Y., Qayyum, M.Z., Pupov, D., Esyunina, D., Kulbachinskiy, A., and Murakami, K.S. (2021). Structural basis of ribosomal RNA transcription regulation. Nat. Commun. *12*, 528. 10.1038/s41467-020-20776-y.

24. Coleman, G.A., Davín, A.A., Mahendrarajah, T.A., Szánthó, L.L., Spang, A., Hugenholtz, P., Szöllősi, G.J., and Williams, T.A. (2021). A rooted phylogeny resolves early bacterial evolution. Science *372*, eabe0511. 10.1126/science.abe0511.

25. Liolos, K., Abt, B., Scheuner, C., Teshima, H., Held, B., Lapidus, A., Nolan, M., Lucas, S., Deshpande, S., Cheng, J.-F., et al. (2013). Complete genome sequence of the halophilic bacterium Spirochaeta africana type strain (Z-7692(T)) from the alkaline Lake Magadi in the East African Rift. Stand. Genomic Sci. *8*, 165–176. 10.4056/sigs.3607108.

26. Zhilina, T.N., Zavarzin, G.A., Rainey, F., Kevbrin, V.V., Kostrikina, N.A., and Lysenko, A.M. (1996). Spirochaeta alkalica sp. nov., Spirochaeta africana sp. nov., and Spirochaeta asiatica sp. nov., alkaliphilic anaerobes from the Continental Soda Lakes in Central Asia and the East African Rift. Int. J. Syst. Bacteriol. *46*, 305–312. 10.1099/00207713-46-1-305.

27. Boyle, W.K., Hall, L.S., Armstrong, A.A., Dulebohn, D.P., Samuels, D.S., Gherardini, F.C., and Bourret, T.J. (2020). Establishment of an in vitro RNA polymerase transcription system: a new tool to study transcriptional activation in Borrelia burgdorferi. Sci. Rep. *10*, 8246. 10.1038/s41598-020-65104-y.

28. Huang, Y.-H., Trapp, V., Puro, O., Mäkinen, J.J., Metsä-Ketelä, M., Wahl, M.C., and Belogurov, G.A. (2022). Fluorogenic RNA aptamers to probe transcription initiation and co-transcriptional RNA folding by multi-subunit RNA polymerases. Meth. Enzymol. *675*, 207–233. 10.1016/bs.mie.2022.07.010.

29. Bremer, H., and Dennis, P.P. (2008). Modulation of chemical composition and other parameters of the cell at different exponential growth rates. Ecosal Plus *3*, 1–49. 10.1128/ecosal.5.2.3.

30. Ross, W., Thompson, J.F., Newlands, J.T., and Gourse, R.L. (1990). E.coli Fis protein activates ribosomal RNA transcription in vitro and in vivo. EMBO J. *9*, 3733–3742. 10.1002/j.1460-2075.1990.tb07586.x.

31. Stallings, C.L., Stephanou, N.C., Chu, L., Hochschild, A., Nickels, B.E., and Glickman, M.S. (2009). CarD is an essential regulator of rRNA transcription required for Mycobacterium tuberculosis persistence. Cell *138*, 146–159. 10.1016/j.cell.2009.04.041.

32. Leschine, S.B., and Canale-Parola, E. (1986). Rifampin-resistant RNA polymerase in spirochetes. FEMS Microbiology Letters *35*, 199–204.

33. Alekshun, M., Kashlev, M., and Schwartz, I. (1997). Molecular cloning and characterization of Borrelia burgdorferi rpoB. Gene *186*, 227–235. 10.1016/s0378-1119(96)00714-7.

34. Bae, B., Chen, J., Davis, E., Leon, K., Darst, S.A., and Campbell, E.A. (2015). CarD uses a minor groove wedge mechanism to stabilize the RNA polymerase open promoter complex. eLife *4*, e08505. 10.7554/eLife.08505.

35. Lilic, M., Darst, S.A., and Campbell, E.A. (2021). Structural basis of transcriptional activation by the Mycobacterium tuberculosis intrinsic antibiotic-resistance transcription factor WhiB7. Mol. Cell *81*, 2875-2886.e5. 10.1016/j.molcel.2021.05.017.

36. Boyaci, H., Chen, J., Jansen, R., Darst, S.A., and Campbell, E.A. (2019). Structures of an RNA polymerase promoter melting intermediate elucidate DNA unwinding. Nature *565*, 382–385. 10.1038/s41586-018-0840-5.

37. Ederth, J., Artsimovitch, I., Isaksson, L.A., and Landick, R. (2002). The downstream DNA jaw of bacterial RNA polymerase facilitates both transcriptional initiation and pausing. J. Biol. Chem. *277*, 37456–37463. 10.1074/jbc.M207038200.

38. Wigneshweraraj, S.R., Burrows, P.C., Severinov, K., and Buck, M. (2005). Stable DNA opening within open promoter complexes is mediated by the RNA polymerase beta'-jaw domain. J. Biol. Chem. *280*, 36176–36184. 10.1074/jbc.M506416200.

39. Campbell, E.A., Muzzin, O., Chlenov, M., Sun, J.L., Olson, C.A., Weinman, O., Trester-Zedlitz, M.L., and Darst, S.A. (2002). Structure of the bacterial RNA

polymerase promoter specificity sigma subunit. Mol. Cell *9*, 527–539. 10.1016/s1097-2765(02)00470-7.

40. Murakami, K.S. (2013). X-ray crystal structure of Escherichia coli RNA polymerase σ70 holoenzyme. J. Biol. Chem. *288*, 9126–9134. 10.1074/jbc.M112.430900.

41. Bae, B., Davis, E., Brown, D., Campbell, E.A., Wigneshweraraj, S., and Darst, S.A. (2013). Phage T7 Gp2 inhibition of Escherichia coli RNA polymerase involves misappropriation of σ70 domain 1.1. Proc Natl Acad Sci USA *110*, 19772–19777. 10.1073/pnas.1314576110.

42. Saecker, R.M., Mueller, A.U., Malone, B., Chen, J., Budell, W.C., Dandey, V.P., Maruthi, K., Mendez, J.H., Molina, N., Eng, E.T., et al. (2024). Early intermediates in bacterial RNA polymerase promoter melting visualized by time-resolved cryo-electron microscopy. Nat. Struct. Mol. Biol. *31*, 1778–1788. 10.1038/s41594-024-01349-9.

43. Henry, K.K., Ross, W., Myers, K.S., Lemmer, K.C., Vera, J.M., Landick, R., Donohue, T.J., and Gourse, R.L. (2020). A majority of Rhodobacter sphaeroides promoters lack a crucial RNA polymerase recognition feature, enabling coordinated transcription activation. Proc Natl Acad Sci USA *117*, 29658–29668. 10.1073/pnas.2010087117.

44. Boyle, W.K., Groshong, A.M., Drecktrah, D., Boylan, J.A., Gherardini, F.C., Blevins, J.S., Samuels, D.S., and Bourret, T.J. (2019). DksA Controls the Response of the Lyme Disease Spirochete Borrelia burgdorferi to Starvation. J. Bacteriol. *201*, e00582-18. 10.1128/JB.00582-18.

45. Mason, C., Thompson, C., and Ouyang, Z. (2020). DksA plays an essential role in regulating the virulence of Borrelia burgdorferi. Mol. Microbiol. *114*, 172–183. 10.1111/mmi.14504.

46. Boyle, W.K., Richards, C.L., Dulebohn, D.P., Zalud, A.K., Shaw, J.A., Lovas, S., Gherardini, F.C., and Bourret, T.J. (2021). DksA-dependent regulation of RpoS contributes to Borrelia burgdorferi tick-borne transmission and mammalian infectivity. PLoS Pathog. *17*, e1009072. 10.1371/journal.ppat.1009072.

47. Goldstein, B.P. (2014). Resistance to rifampicin: a review. J. Antibiot. *67*, 625–630. 10.1038/ja.2014.107.

48. Rasouly, A., Shamovsky, Y., Epshtein, V., Tam, K., Vasilyev, N., Hao, Z., Quarta, G., Pani, B., Li, L., Vallin, C., et al. (2021). Analysing the fitness cost of antibiotic resistance to identify targets for combination antimicrobials. Nat. Microbiol. *6*, 1410–1423. 10.1038/s41564-021-00973-1.

49. Li, L., Molodtsov, V., Lin, W., Ebright, R.H., and Zhang, Y. (2020). RNA extension drives a stepwise displacement of an initiation-factor structural module in initial transcription. Proc Natl Acad Sci USA *117*, 5801–5809. 10.1073/pnas.1920747117.

50. Brewer, J., Delbeau, M., Zoullas, W.B., Darst, S.A., and Campbell, E.A. (2025). Structural Insights into De Novo Promoter Escape by Mycobacterium tuberculosis RNA Polymerase. Nat. Commun. *16*, 9990. 10.1038/s41467-025-64941-7.

51. Wang, F., Redding, S., Finkelstein, I.J., Gorman, J., Reichman, D.R., and Greene, E.C. (2013). The promoter-search mechanism of Escherichia coli RNA polymerase is dominated by three-dimensional diffusion. Nat. Struct. Mol. Biol. *20*, 174–181. 10.1038/nsmb.2472.

52. Friedman, L.J., Mumm, J.P., and Gelles, J. (2013). RNA polymerase approaches its promoter without long-range sliding along DNA. Proc Natl Acad Sci USA *110*, 9740–9745. 10.1073/pnas.1300221110.

53. Tchamedeu Kameni, A.-P., Couture-Tosi, E., Saint-Girons, I., and Picardeau, M. (2002). Inactivation of the spirochete recA gene results in a mutant with low viability and irregular nucleoid morphology. J. Bacteriol. *184*, 452–458. 10.1128/JB.184.2.452-458.2002.

54. Kanehisa, M., Sato, Y., Kawashima, M., Furumichi, M., and Tanabe, M. (2016). KEGG as a reference resource for gene and protein annotation. Nucleic Acids Res. *44*, D457-62. 10.1093/nar/gkv1070.

55. Edgar, R.C. (2004). MUSCLE: multiple sequence alignment with high accuracy and high throughput. Nucleic Acids Res. *32*, 1792–1797. 10.1093/nar/gkh340.

56. Castresana, J. (2000). Selection of conserved blocks from multiple alignments for their use in phylogenetic analysis. Mol. Biol. Evol. *17*, 540–552. 10.1093/oxfordjournals.molbev.a026334.

57. Huelsenbeck, J.P., and Ronquist, F. (2001). MRBAYES: Bayesian inference of phylogenetic trees. Bioinformatics *17*, 754–755. 10.1093/bioinformatics/17.8.754.

58. Jones, D.T., Taylor, W.R., and Thornton, J.M. (1992). The rapid generation of mutation data matrices from protein sequences. Comput. Appl. Biosci. *8*, 275–282. 10.1093/bioinformatics/8.3.275.

59. Yang, Z. (1994). Maximum likelihood phylogenetic estimation from DNA sequences with variable rates over sites: approximate methods. J. Mol. Evol. *39*, 306–314. 10.1007/BF00160154.

60. Gouy, M., Guindon, S., and Gascuel, O. (2010). SeaView version 4: A multiplatform graphical user interface for sequence alignment and phylogenetic tree building. Mol. Biol. Evol. *27*, 221–224. 10.1093/molbev/msp259.

61. Okonechnikov, K., Golosova, O., Fursov, M., and UGENE team (2012). Unipro UGENE: a unified bioinformatics toolkit. Bioinformatics *28*, 1166–1167. 10.1093/bioinformatics/bts091.

62. Jumper, J., Evans, R., Pritzel, A., Green, T., Figurnov, M., Ronneberger, O., Tunyasuvunakool, K., Bates, R., Žídek, A., Potapenko, A., et al. (2021). Highly accurate protein structure prediction with AlphaFold. Nature *596*, 583–589. 10.1038/s41586-021-03819-2.

63. Varadi, M., Bertoni, D., Magana, P., Paramval, U., Pidruchna, I., Radhakrishnan, M., Tsenkov, M., Nair, S., Mirdita, M., Yeo, J., et al. (2024). AlphaFold Protein Structure Database in 2024: providing structure coverage for over 214 million protein sequences. Nucleic Acids Res. *52*, D368–D375. 10.1093/nar/gkad1011.

64. Abramson, J., Adler, J., Dunger, J., Evans, R., Green, T., Pritzel, A., Ronneberger, O., Willmore, L., Ballard, A.J., Bambrick, J., et al. (2024). Accurate structure prediction of biomolecular interactions with AlphaFold 3. Nature *630*, 493–500. 10.1038/s41586-024-07487-w.

65. Filonov, G.S., Moon, J.D., Svensen, N., and Jaffrey, S.R. (2014). Broccoli: rapid selection of an RNA mimic of green fluorescent protein by fluorescence-based selection and directed evolution. J. Am. Chem. Soc. *136*, 16299–16308. 10.1021/ja508478x.

66. Studier, F.W. (2005). Protein production by auto-induction in high density shaking cultures. Protein Expr. Purif. *41*, 207–234. 10.1016/j.pep.2005.01.016.

67. Svetlov, V., and Artsimovitch, I. (2015). Purification of bacterial RNA polymerase: tools and protocols. Methods Mol. Biol. *1276*, 13–29. 10.1007/978-1-4939-2392-2_2.

68. Fitzgerald, D.J., Berger, P., Schaffitzel, C., Yamada, K., Richmond, T.J., and Berger, I. (2006). Protein complex expression by using multigene baculoviral vectors. Nat. Methods *3*, 1021–1032. 10.1038/nmeth983.

69. Abramoff, M.D., Magalhaes, P.J., and Ram, S.J. (2004). Image processing with ImageJ. Biophotonics International *11*, 36–42.

70. Punjani, A., Rubinstein, J.L., Fleet, D.J., and Brubaker, M.A. (2017). cryoSPARC: algorithms for rapid unsupervised cryo-EM structure determination. Nat. Methods *14*, 290–296. 10.1038/nmeth.4169.

71. Punjani, A., Zhang, H., and Fleet, D.J. (2020). Non-uniform refinement: adaptive regularization improves single-particle cryo-EM reconstruction. Nat. Methods *17*, 1214–1221. 10.1038/s41592-020-00990-8.

72. Grigorieff, N. (2016). Frealign: An Exploratory Tool for Single-Particle Cryo-EM. Meth. Enzymol. *579*, 191–226. 10.1016/bs.mie.2016.04.013.

73. Casañal, A., Lohkamp, B., and Emsley, P. (2020). Current developments in Coot for macromolecular model building of Electron Cryo-microscopy and Crystallographic Data. Protein Sci. *29*, 1069–1078. 10.1002/pro.3791.

74. Emsley, P., and Cowtan, K. (2004). Coot: model-building tools for molecular graphics. Acta Crystallogr. D Biol. Crystallogr. *60*, 2126–2132. 10.1107/S0907444904019158.

75. Adams, P.D., Afonine, P.V., Bunkóczi, G., Chen, V.B., Echols, N., Headd, J.J., Hung, L.-W., Jain, S., Kapral, G.J., Grosse Kunstleve, R.W., et al. (2011). The Phenix software for automated determination of macromolecular structures. Methods *55*, 94–106. 10.1016/j.ymeth.2011.07.005.

76. Afonine, P.V., Poon, B.K., Read, R.J., Sobolev, O.V., Terwilliger, T.C., Urzhumtsev, A., and Adams, P.D. (2018). Real-space refinement in PHENIX for cryo-EM and crystallography. Acta Crystallogr. D Struct. Biol. *74*, 531–544. 10.1107/S2059798318006551.

77. Williams, C.J., Headd, J.J., Moriarty, N.W., Prisant, M.G., Videau, L.L., Deis, L.N., Verma, V., Keedy, D.A., Hintze, B.J., Chen, V.B., et al. (2018). MolProbity: more and better reference data for improved all-atom structure validation. Protein Sci. *27*, 293–315. 10.1002/pro.3330.

78. Pettersen, E.F., Goddard, T.D., Huang, C.C., Meng, E.C., Couch, G.S., Croll, T.I., Morris, J.H., and Ferrin, T.E. (2021). UCSF ChimeraX: structure visualization for researchers, educators, and developers. Protein Sci. *30*, 70–82. 10.1002/pro.3943.

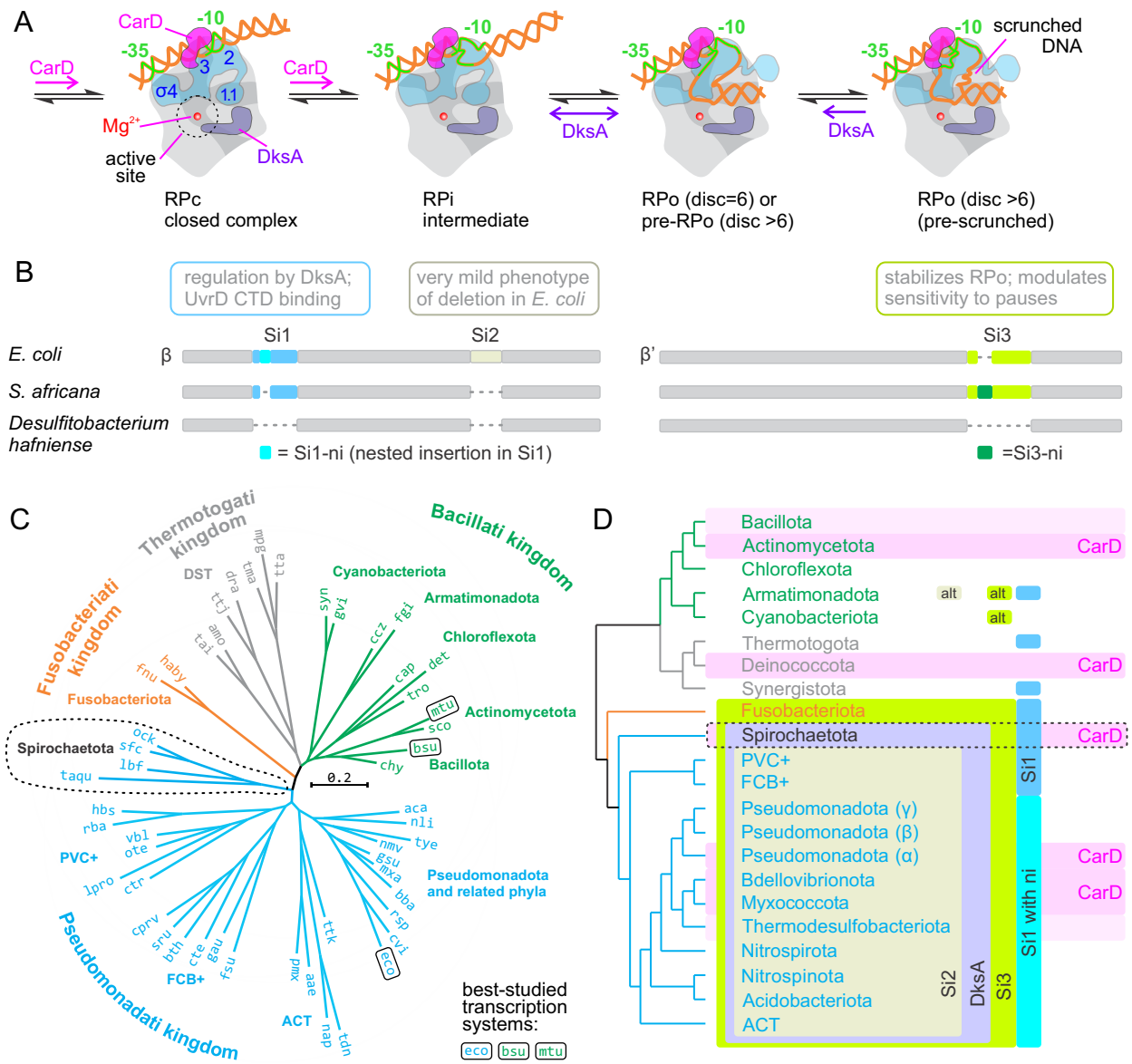

Figure 1. Spirochaetota is a deeply rooted phylum featuring a unique combination of lineage-specific inserts in RNAP and transcription initiation factors. (A) A simplified and abbreviated schematics of promoter recognition and melting by the primary RNAP holoenzyme. CarD helps anchoring the upstream DNA and facilitates melting of the -10 promoter element. DksA modulates the downstream DNA loading and promoter pre-scrunching. (B) The schematics depicting the location of Si1, Si2 and Si3 inserts in the primary sequences of β and β' subunits of *E. coli* and *S. africana* RNAPs. *E. coli* Si1 and *S. africana* Si3 contain nested inserts, Si1-ni and Si3-ni, respectively. Insert-less RNAP from Bacillota is shown as a reference. (C) Bayesian molecular phylogenetic tree inferred using alignment of concatenated RNAP subunits and NusA transcription factor. Species names are described in **Table S1**. (D) The distribution of lineage specific inserts and transcription initiation factors CarD and DksA. The presence of factors is designated only for phyla where CarD and DksA are highly prevalent. Light pink shading: CarD is frequently found but not prevalent. "alt" signifies the presence of sequence inserts that positionally correspond but are not homologous to Si2 and Si3 inserts of *E. coli* RNAP.

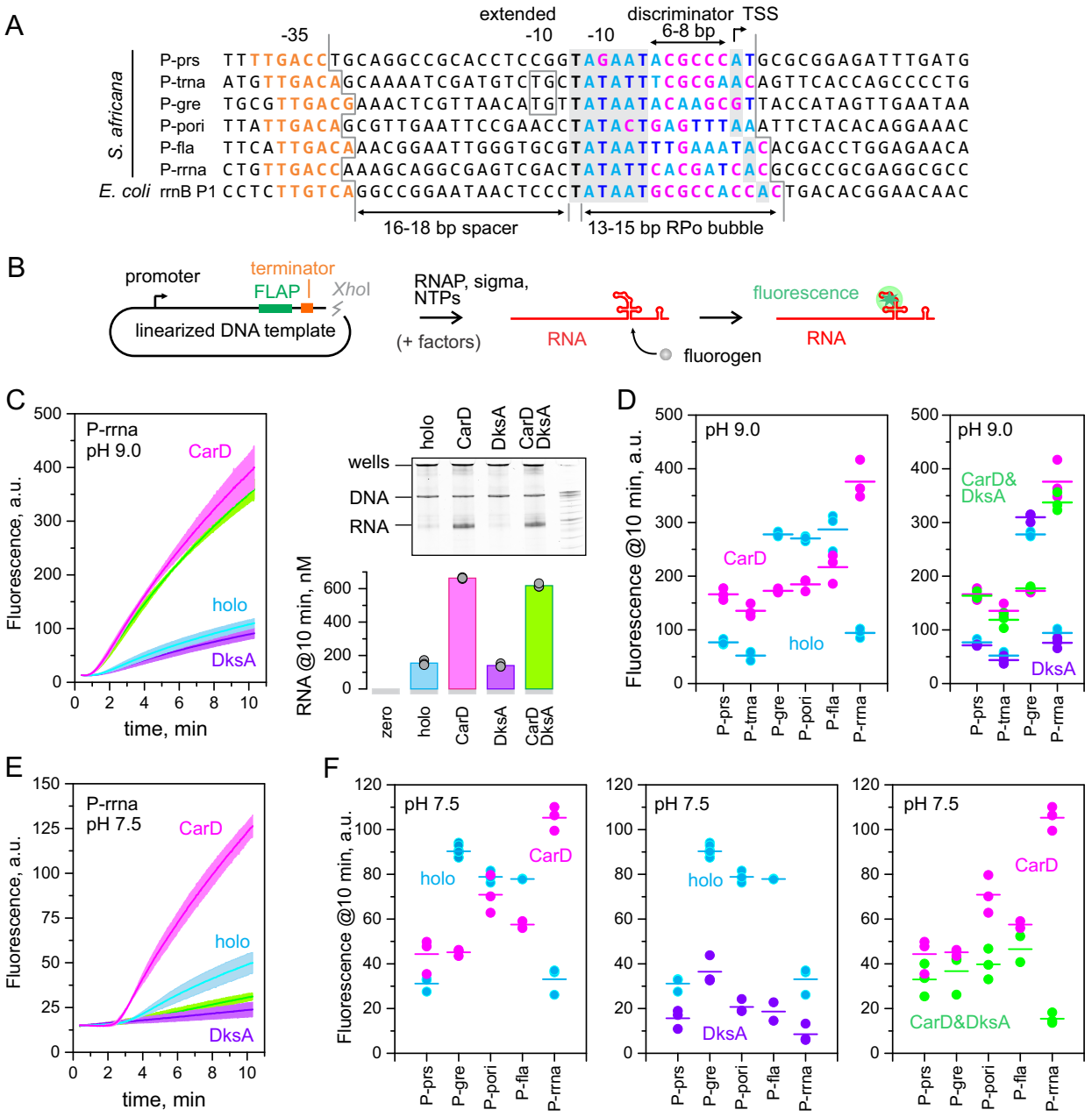

Figure 2. The effects of CarD and DksA on transcription initiation by *S. africana* RNAP holoenzyme. (A) Sequences of promoters used in this study aligned by -10 elements. (B) The schematic of the multi-round transcription assay using fluorescent light up aptamer (FLAP). (C) Transcription activity of the P-rrna promoter at pH 9.0. Real-time monitoring of transcription using FLAP (left graph), RNA concentration measured by Qubit assay (bar graph), SYBR-Gold stained denaturing PAGE gel (at 10 min). (D) Effects of CarD, DksA and their combination on transcription activity of six spirochetal promoters at pH 9.0. (E) Real-time monitoring of transcription from the P-rrna promoter at pH 7.5. (F) Effects of CarD, DksA and their combination on transcription activity of five spirochetal promoters at pH 7.5. Transcription assays were performed at 37 °C using 1 μM RNAP, 4 μM σ, 50 nM DNA template and where indicated 10 μM CarD and/or DksA. Bars in (D) and (F) indicate averages of three independent experiments.

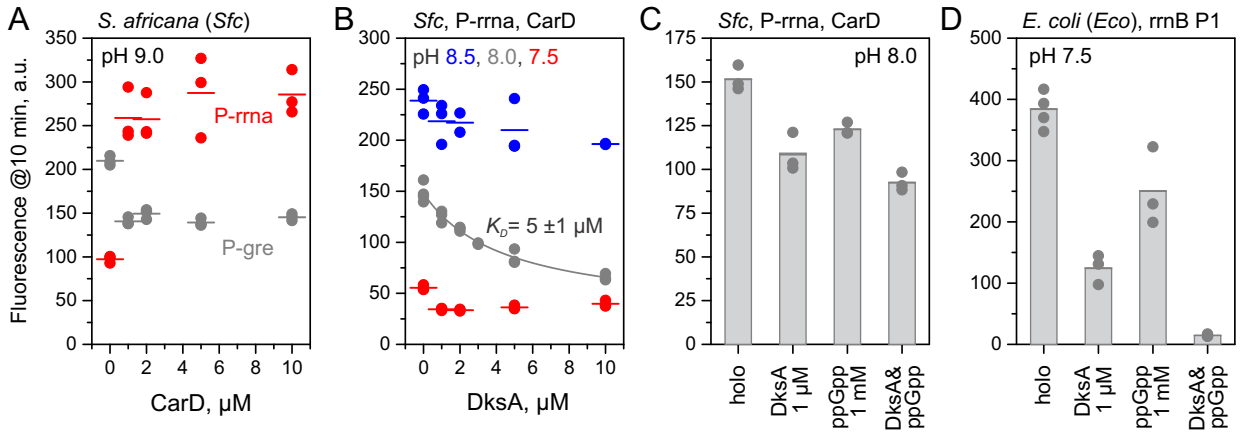

Figure 3. Concentration dependence of CarD and DksA effects on transcription activity of *S. africana* RNAP holoenzyme. (A) Modulation of P-gre and P-rrna activity by CarD as a function of CarD concentration. (B) The effect of DksA on transcription from the P-rrna promoter as a function of DksA concentration. CarD was present at 10 μM. The gray line is the bestfit to the hyperbolic equation. (C) Additive effect of ppGpp and DksA on transcription from the P-rrna promoter at pH 8.0. CarD was present at 2 μM. (D) Synergistic effect of ppGpp and *E. coli* DksA on transcription from rrnB P1 by *E. coli* holoenzyme at pH 7.5 (control experiment). Transcription assays were performed at 37 °C using 0.5 μM RNAP, 10 μM (in A-B) or 4 μM (in C-D) σ, 50 nM DNA template. Bars indicate averages of three independent experiments.

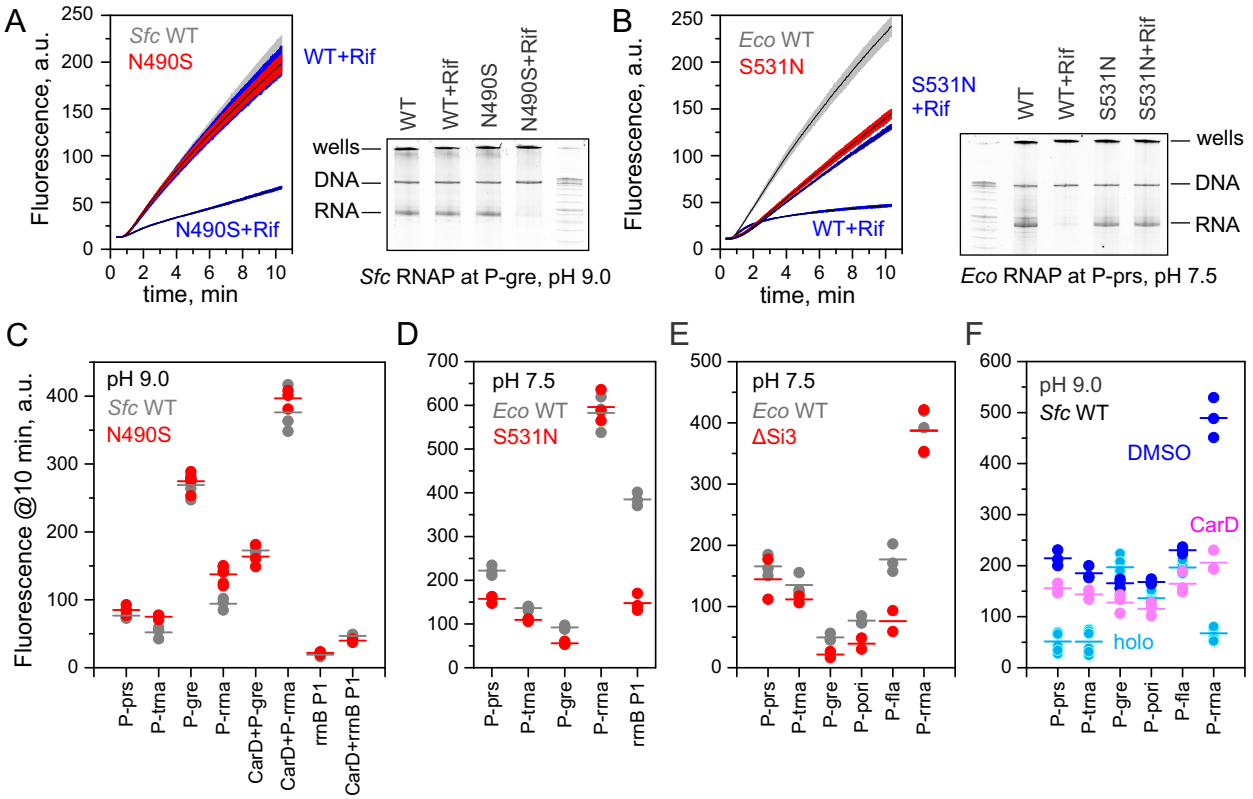

Figure 4. Resistance to rifampicin does not govern the promoter preferences of *S. africana* RNAP. (A) The effect of 1 μM of rifampicin on transcription by the wild-type and βN490S variant of *S. africana* holoenzyme at P-gre promoter. Left: real-time monitoring of transcription using FLAP assay. Right: transcription reactions were incubated for 10 min, reaction products were resolved on 6% denaturing PAGE gel and stained with SYBR-Gold. (B) The effect of 1 μM of rifampicin on transcription by the wild-type and βS351N variant of *E. coli* holoenzyme at P-prs promoter. (C) The effect of βN490S substitution on the promoter preferences of *S. africana* holoenzyme. (D) The effect of βS531N substitution on the promoter preferences of *E. coli* holoenzyme. (E) The effect of deletion of Si3 on the promoter preferences of *E. coli* holoenzyme. (F) The effect of 10% DMSO on the promoter preferences of *S. africana* holoenzyme. Transcription assays were performed at 37 °C using 1 μM RNAP, 4 μM σ, 50 nM DNA template at pH 9.0 (*S. africana*) and pH 7.5 (*E. coli*). CarD was added at 10 μM where indicated. Measurements in (E) and (F) were performed using end-point-only FLAP assay. Fluorescence readings were scaled × 1.5 fold to account for the dilution during quenching by fluorogen-EDTA mixture. Bars indicate averages of three independent experiments.

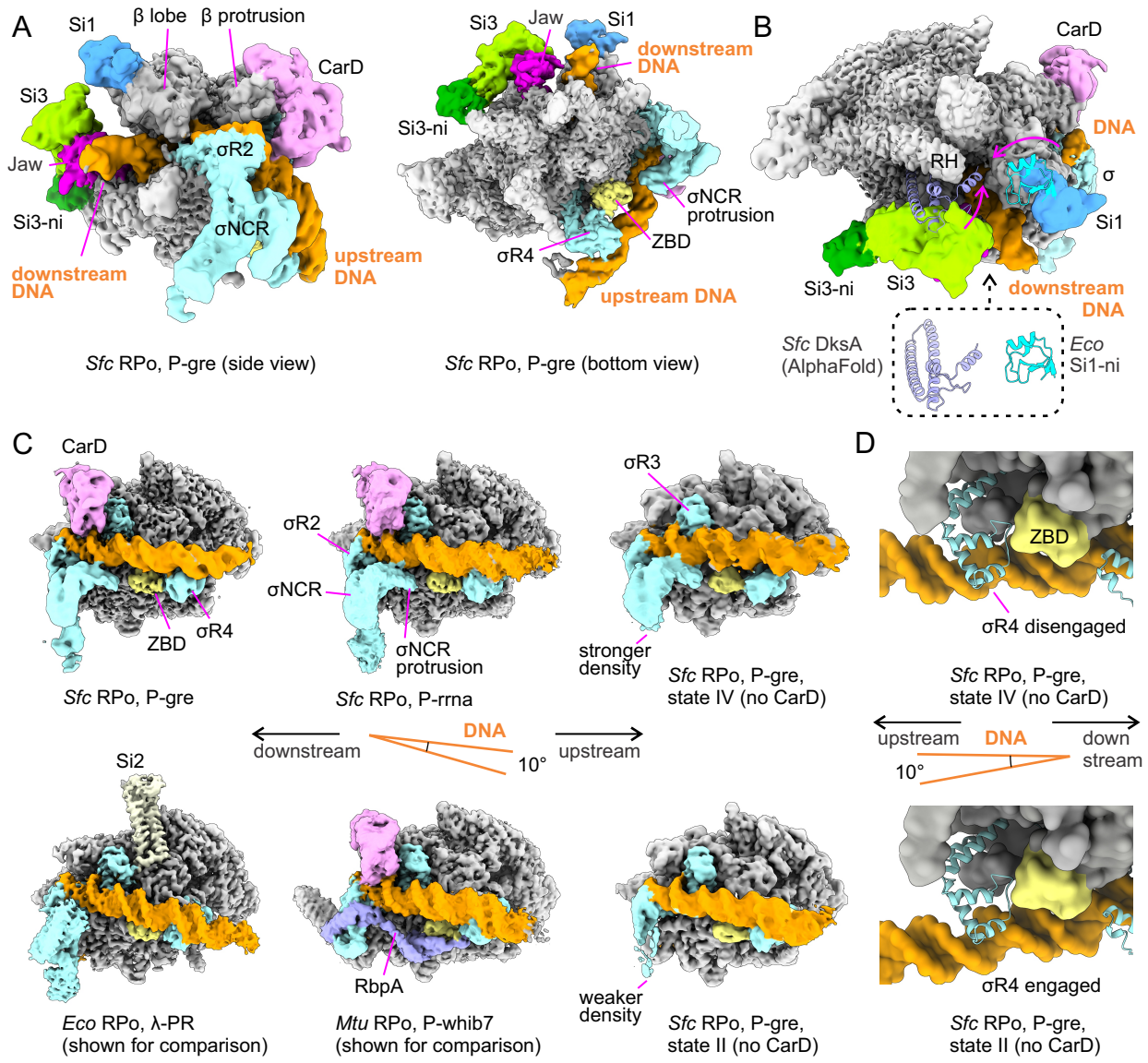

Figure 5. Structures of the *S. africana* RPo at P-gre and P-rrna promoters. (A) CarD binds to β protrusion and upstream DNA in a canonical conformation previously observed for mycobacterial CarD. Si3 insert positions the Jaw domain to interact with the downstream DNA. (B) Si1 is positioned far away from all other RNAP domains. The *E. coli* Si1-ni subdomain (blue cartoon) and *S. africana* DksA (purple cartoons) are modeled-in based on the alignment with *E. coli* holoenzyme structures. Magenta arrows indicate motions of lobe and Si3 domains that bring *Eco* Si1-ni in contact with either Si3 (PDB ID 5IPN) or DksA (PDB ID 7KHI). RH, β' Rim Helices. (C) The overall course of the upstream DNA in *S. africana* RPo. *E. coli* (PDB ID 7MKD) and *M. tuberculosis* (PDB ID 7KIN) RPo are shown for comparison. The top row displays structures where the -35 promoter promoter element is disengaged from σR4, whereas the bottom row displays canonical engaged conformations. (D) Close-up view of the disengaged (top) and engaged (bottom) conformations of the upstream DNA in *S. africana* RPo. Structures in (C) and (D) were aligned using the β subunit as a reference. The central schematics highlight the differing paths of the upstream DNA between the top and bottom structures.

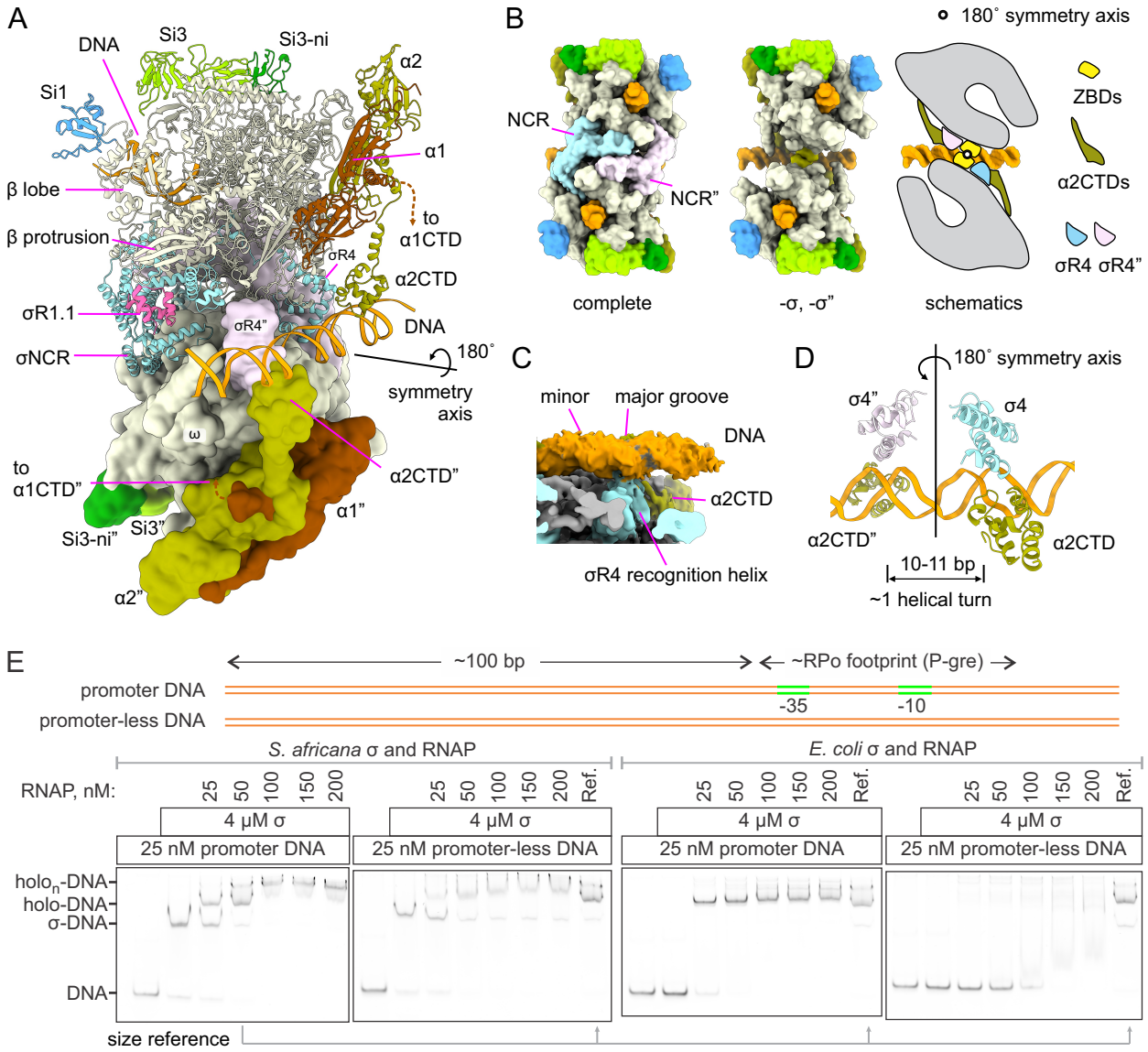

Figure 6. *S. africana* holoenzyme dimer bound to DNA in a non-sequence-specific manner. (A) The top protomer and DNA duplexes are shown as cartoons, the bottom protomer is depicted as a surface. The σ subunits are colored light cyan (top protomer), and light pink (bottom protomer). (B) A view along the axis of the DNA end-bound within the downstream DNA channel. Both protomers are shown as surfaces. The left projection shows the complete structure. The middle projection omits σ subunits to reveal the juxtaposed ZBDs at the interface between the protomers. The right schematic visualizes the core architecture of the complex. (C) Cut-out view illustrating the engagement of the minor groove of DNA by σR4. (D) Close-up view illustrating the engagement of the minor DNA groove by σR4 and α2CTD. (E) Electrophoretic mobility shift assay (EMSA) was used to assess the binding of *S. africana* and *E. coli* holoenzymes to DNA fragments with and without a promoter at submicromolar concentrations of RNAP and DNA.

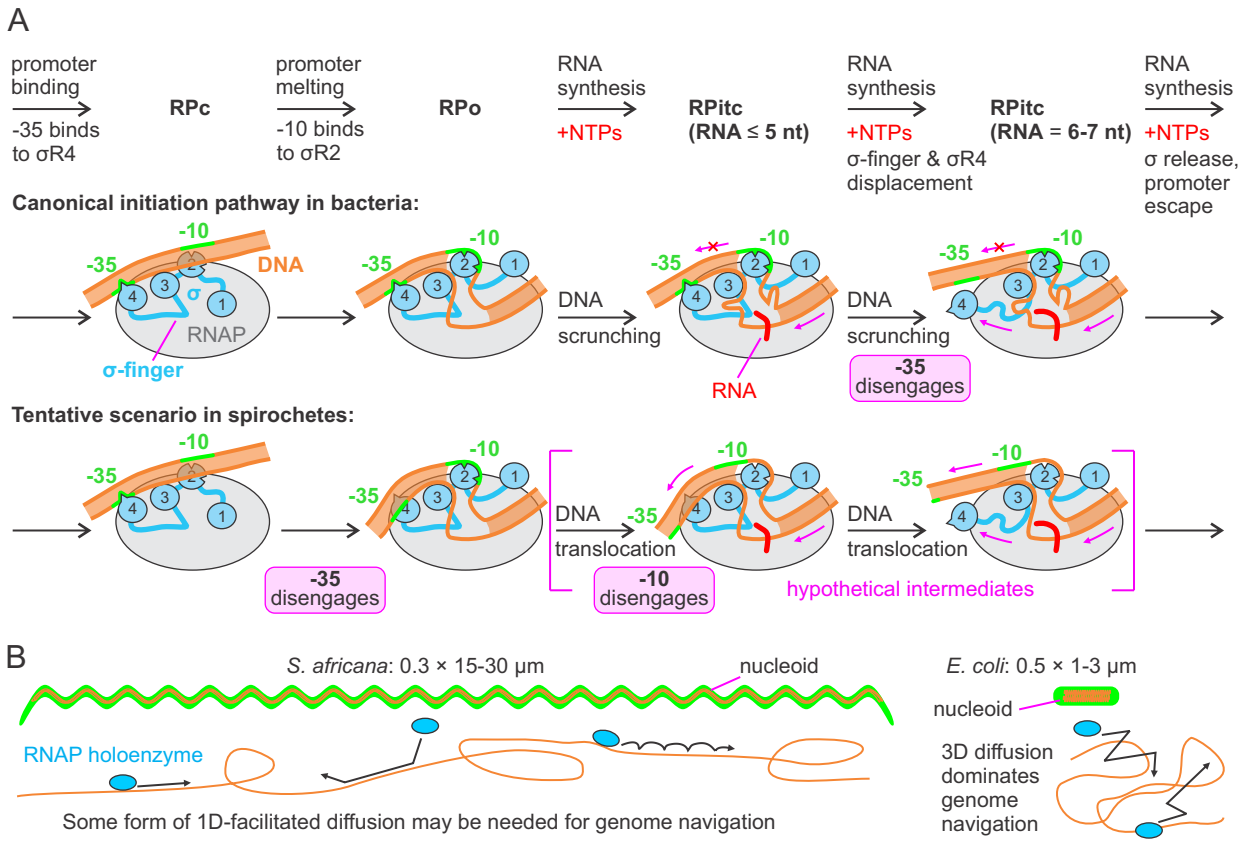

Figure 7. Distinctive features of the spirochetal transcription apparatus. (A) Bacterial RNAP holoenzymes typically disengage the -35 promoter element after synthesizing RNA six or more nucleotides long (top schematic). In the spirochetal system, the coupling of -35 disengagement with promoter melting may facilitate the earlier release of the -10 promoter element during the initial transcription, leading to a promoter escape pathway with less DNA scrunching (bottom schematic). Magenta arrows indicate the movement of DNA, σ-finger and σR4, or lack of movement (if crossed). (B) Schematic comparison of the cell morphology of *S. africana* and *E. coli* provides a rationale for the tighter non-sequence-specific association of the spirochetal holoenzyme with DNA.

Supplementary Information

Regulatory landscapes and structural choreography of transcription initiation in spirochetes

Vilma K. Trapp[†], Tingting Wang[†], Tarek Hilal, Janne J. Makinen, Juho Kotikoski, Paavo J. Tavi, Ville Levola, Sari Paavilainen, Bernhard Loll, Markus C. Wahl*, Georgiy A. Belogurov*

[†] Shared first authors; these authors contributed equally to this work.

* Correspondence to: markus.wahl@fu-berlin.de; gebelo@utu.fi

Supplementary methods

S. africana cultivation

S. africana was routinely cultivated in an alkali medium (pH 9.2-9.5) modified from the DSMZ alkaliphilic spirochaete medium #700. The medium was buffered by a mixture of Na_2CO_3 (10 g/l) and $NaHCO_3$ (15 g/l), contained NaCl (50 g/l) to maintain high-salinity [1], maltose (5 g/l) as a major carbon and energy source and Na_2S (0.5 g/l) and cysteine hydrochloride (0.5 g/l) as reducing agents. The medium also contained NH_4Cl (0.5 g/l), K_2HPO_4 (0.5 g/l), yeast extract (0.5 g/l), 10 ml/l of vitamin solution, 1 ml/l of trace element solution and 1 mg/l of resazurin as redox indicator. For cultivation at pH 8.5, $NaHCO_3$ was increased to 25 g/l and Na_2CO_3 was omitted. For monitoring the survival at pH 7.5, HEPES-Na (HEPES 12 g/l, NaOH 1 g/l) was used as a buffering agent, Na_2CO_3 and $NaHCO_3$ were omitted, and NaCl was increased to 90 g/l.

A continuous culture was grown in completely filled 6.5 ml soda-lime glass tubes with polypropylene screw caps and thermoplastic elastomer seal (or up to 1 l screw caps bottles when desired) without shaking at 25°C, pH 9.2-9.5 and transferred every 3 days (OD_{600} 0.3-0.5; 25 µl to 6.5 ml). Alternatively, 3-day old cultures were supplemented with glycerol (16% final), stored at -80°C and revived when desired. On day 4 cultures reached saturating OD_{600} ~0.8, cells maintained spiral shape and motility, and the culture remained evenly turbid. On day 5 culture health deteriorated, a large fraction of cells sedimented to the bottom of the tube and morphed into spherical bodies. When grown at 30°C, cultures reached saturation on day 3 and the viability deteriorated on day 4. When grown at 25°C, pH 8.5, cultures reached saturation on day 7 and remained healthy on day 12 after which the viability rapidly deteriorated. When 3-day old cultures pre-grown at pH 9.2-9.5 were pelleted and transferred to pH 7.5 medium, cells remained spiral and motile on day 2 followed by the massive die out on days 3-4, but a small number of spiral and motile cells were observed up to at least day 7.

MODIFIED ALKALIPHILIC SPIROCHAETE MEDIUM

Main solution

10	g	Na_2CO_3
15	g	$NaHCO_3$
50	g	NaCl
0.5	g	K_2HPO_4
0.5	g	NH_4Cl
0.5	g	Cysteine hydrochloride
0.5	g	Na_2S x 9 H_2O
0.5	g	Yeast extract
5	g	Maltose
1	mg	Resazurin
10	ml	**Wolin's vitamin solution**
1	ml	**Modified Wolin's mineral solution II**
1000	ml	Distilled water

Filter sterilize, warm up to 60 C and cool down to room temperature. Expected pH 9.2-9.5

Modified Wolin's mineral solution II

1.5	g	Nitrilotriacetic acid
3	g	$MgSO_4$ x 7 H_2O
0.5	g	$MnSO_4$ x H_2O
1	g	NaCl
0.1	g	$FeSO_4$ x 7 H_2O
0.18	g	$CoSO_4$ x 7 H_2O
0.1	g	$CaCl_2$ x 2 H_2O
0.18	g	$ZnSO_4$ x 7 H_2O
0.01	g	$CuSO_4$ x 5 H_2O
0.02	g	$AlK(SO_4)_2$ x 12 H_2O
0.01	g	H_3BO_3
0.01	g	Na_2MoO_4 x 2 H_2O
0.025	g	$NiCl_2$ x 6 H_2O
0.3	mg	Na_2SeO_3 x 5 H_2O
1000	ml	Distilled water

First dissolve nitrilotriacetic acid and adjust pH to 6.5 with KOH, then add minerals. Adjust final to pH 7.0 with KOH.

Wolin's vitamin solution

2	mg	Biotin
2	mg	Folic acid
10	mg	Pyridoxine hydrochloride
5	mg	Thiamine HCl
5	mg	Riboflavin
5	mg	Nicotinic acid
5	mg	Calcium D-(+)-pantothenate
0.1	mg	Vitamin B12
5	mg	p-Aminobenzoic acid
5	mg	(DL)-alpha-Lipoic acid
1000	ml	Distilled water

Purification of *S. africana* RNAP from *S. africana* cells

Native *S. africana* RNAP was purified from *S. africana* cells by a combination of heparin, size-exclusion and anion exchange chromatography. *S. africana* cultures were grown for 3-4 days at 25-30°C until the early saturation at OD_{600} ~0.8 (6.5 ml inoculum per 1 l bottle of standard medium with pH 9.2-9.5). *S. africana* cells were harvested by centrifugation at 10,000 × g for 30 min at 4°C (~15 g from 6 l of culture, stored at -80°C), resuspended in 10% Buffer B supplemented with EDTA-free protease inhibitor cocktail (Pierce or Roche) and disrupted by a mild sonication. At least 30 ml of lysis buffer was used per 5 g of cells. Lysates were clarified by centrifugation at 40-60,000 × g for 0.5-1 h at 4°C and loaded onto a 5 ml HiTrap® Heparin HP column (Cytiva) equilibrated with 10% Buffer B. The column was washed with 15 ml of 10% Buffer B and proteins were eluted with a steep gradient of Buffer B (30 ml, 10-100%). All protein-containing fractions were pooled, concentrated to 2 ml using a Amicon Ultra-15 (15 ml) centrifugal filter unit with Ultracel-3 (3 kDa cutoff) membrane and loaded onto a 120 ml HiPrep™ Sephacryl™ S-400 HR 16/60 gel filtration column (Cytiva) equilibrated with 10% Buffer B. RNAP eluted from the column between 70 and 80 ml. Fractions containing RNAP were pooled, concentrated using ultrafiltration concentrators, dialyzed against the storage buffer and stored at -20°C (short term) or -80°C (long term). Alternatively, RNAP-containing fractions were loaded onto a 6 ml ResourceQ column (Cytiva) equilibrated with 10% Buffer B, washed with 15-30 ml of 10% buffer B, and RNAP was eluted with a 100 ml gradient of buffer B (10-100%) followed by concentration and dialysis.

Total RNA isolation from *S. africana*

Total cell RNA was isolated using TRIzol® Max™ Bacterial RNA Isolation Kit (Thermofisher). Cells from 6.5 ml culture were harvested by centrifugation at 4,000 × g for 10 min at 4°C and resuspended in 200 µl of Max Bacterial Enhancement Reagent preheated at 95°C. The sample was then dissolved in 1 ml TRIzol and extracted twice with 200 µl of cold chloroform. RNA was then precipitated from the aqueous phase by addition of 500 µl of cold isopropanol. The RNA pellet was washed with 1 ml of 75% ethanol and dissolved in 50 µl of RNase-free water. The sample was then treated with DNase (TURBO DNA-free™ Kit, Thermofisher). Briefly, the sample was supplemented with DNase buffer, DNase, diluted to 100 µl, and incubated for 20 min at 37°C. DNase and divalent cations were then removed by the proprietary DNase removal matrix supplied with the kit. RNA was then additionally cleaned up using Qiagen RNAeasy mini kit using Clean-up protocol. Briefly, the RNA sample was supplemented with 350 µl of high-salt proprietary buffer containing guanidine thiocyanate (Buffer RLT), 950 µl of 99% ethanol (up from the default 250 µl of ethanol to facilitate binding of small RNAs) and applied to the silica-based spin column. The column

was washed with the low-salt proprietary buffer (Buffer RPE) containing 75% ethanol, and RNA was eluted with 50 µl of RNase-free water.

Transcriptome sequencing and analysis

Total RNA was isolated from a 3-day-old *S. africana* culture grown at pH 9.2-9.5 until early saturation (OD_{600} ~0.8) at 30 °C. Total RNA (100 ng) was converted into a dual-indexed library using Illumina® Stranded Total RNA Prep, Ligation with Ribo-Zero Plus kit and sequenced with Illumina NovaSeq 6000 SP v1.5 (2 × 100 bp). The library preparation and RNA sequencing were performed by the Finnish Functional Genomics Centre Facility (FFGC). The RNA sample and library quality were monitored using an Agilent Bioanalyzer 2100 instrument and software (Agilent). The read quality was inspected using FastQC.

The automated transcriptome assembly was conducted using Rockhopper v2.03 [2] that aligned raw reads (FASTQ format) to the annotated *S. africana* DSM8902 genome [3], produced coverage traces (WIG format) and a table containing raw read counts and expression values (analogues of FPKM but normalized by the upper quartile of gene expression, excluding genes with zero expression) for annotated genome features (**Supplementary Data File**). Transcriptome coverage was explored using Integrative Genomics Viewer [4]. For figure preparation, strand-specific transcriptome coverage of selected regions of the genome was extracted from WIG files using a python script and plotted using Origin 2015 software (Origin Labs).

As an alternative analysis method, raw reads (FASTQ format) were mapped to the *S. africana* genome using Bowtie2 v2.5.3 [5]. The resulting alignment in SAM format was sorted and indexed using SAMtools v1.19 [6]. Reads mapping to the genome features (Gene Transfer Format, GTF) were then counted using HTSeq v2.0.3 [7]. The HTSeq read counts were normalized using the transcripts per million (TPM) method (**Supplementary Data File**).

Analysis of *in vitro* transcription products using Oxford nanopore sequencing

To estimate transcription across the entire linearized transcription template (P-gre template was used as an example), *in vitro* transcription was performed as in the FLAP assays, but the reaction volume was scaled up to 0.5 ml and DFHBI-1T was omitted. Product RNAs were purified using the RNA easy kit (Qiagen) and polyadenylated with *E. coli* PAP (poly-A polymerase, NEB) to enable ligation of the sequencing adapters to the 3' ends of the RNAs. RNAs were purified using Agencourt RNAClean XP beads (Beckman Coulter), the sequencing library was prepared using the Direct RNA sequencing kit (Oxford nanopore) and sequenced using a MinION Mk1D instrument (Oxford nanopore). Reads were aligned to the linearized P-gre transcription template using MinKNOW, alignment files were split according to the strand using SAMtools[6], loaded into Ugene[8], strand-specific coverage was exported and ultimately plotted using Origin 2015 software.

In the transcription start site mapping experiment, seven *in vitro* transcription reactions were performed individually, each using a dedicated linearized plasmid template (six plasmids from the main set and the parent pOP004 plasmid featuring P-gre promoter with the altered initially transcribed region). One set of reactions was performed using *S. africana* holoenzyme and another set using *E. coli* holoenzyme. After quenching with EDTA, the product RNAs in each set were pooled together, purified using the RNA easy kit and polyadenylated with *E. coli* PAP. Polyadenylated RNAs were then bound to Oligo-d(T)25 magnetic beads (NEB) in the presence of 0.5 M LiCl and treated with RppH (RNA pyrophosphohydrolase, NEB) to convert 5' triphosphate moieties into single phosphate moieties. A 24 nt RNA adapter (CACACGCACACACAACCAGAGGAG) was then ligated to the 5' ends of the product RNAs by T4 RNA ligase I (NEB) in the presence of 12.5% (v/v) PEG. RNAs were released from beads by heating to 75 °C for 2 min. RNAs were purified using Agencourt RNAClean XP beads, the sequencing library was prepared using the Direct RNA sequencing kit (Oxford nanopore) and sequenced using a MinION Mk1D instrument (Oxford nanopore).

The reference RNA sequences were constructed for each of the seven promoters assuming that transcription initiates at a purine separated by 6 or 7 bp from the -10 promoter element or at a purine separated by 7 bp from the -10 element if the former is not present. Reads (FASTQ format) were aligned to the reference RNAs using MinKNOW (BAM format output). The default alignment settings in MinKNOW are relaxed enough to recover reads with small indels at the adapter-RNA 5' junction and the same reads were recovered if the reference sequences were constructed using transcription start sites ±2 nucleotides. Reads that overlap with the adapter sequence (first 24 nt) were extracted (BAM format output) and converted back to a FASTQ format list using SAMtools. Reads were then loaded into Ugene and searched with sequence patterns containing 6 nucleotides of the adapter and 7 nucleotides of RNA transcribed from the predicted transcription start site ±2 nucleotides. Additional patterns were designed after slippage was detected by manual inspection of read alignments. To perform the manual inspection, extracted reads were realigned to the reference RNAs using Muscle [9] to reveal sequence insertions that are obscured when viewing BAM format alignments.

In vitro crosslinking with DSSO followed by mass spectrometry analysis

S. africana holoenzyme (100 µl, 15 µM) with and without CarD (15 µM) was dialyzed against high-salt phosphate buffered saline (PBS; pH 7.4, 300 mM NaCl) resulting in 150 µl of 10 µM solution. Proteins were crosslinked with 3 mM disuccinimidyl sulfoxide (DSSO) for 30 min at 25 °C, quenched with Tris-HCl pH 7.9 (30 mM final) and dialyzed against PBS (pH 7.6, 150 mM NaCl). Samples were treated with urea, proteins were reduced with 10 mM dithiothreitol (in 50 mM Tris-HCl, pH 8.0), alkylated with 40 mM iodoacetamide and

digested overnight with sequencing grade modified trypsin (Promega). Peptides were desalted using Sep-Pak tC18 96-well plate (Waters) and dried in a vacuum centrifuge. The dried peptide samples were dissolved with 0.1% formic acid and 1500 ng were subjected to the Liquid Chromatography-Electrospray Ionization-Tandem Mass Spectrometry (LC-ESI-MS/MS) analysis. The LC-ESI-MS/MS analyses were performed on a nanoflow HPLC system (Easy-nLC1000, Thermo Scientific) coupled to the Orbitrap Fusion Lumos mass spectrometer (Thermo Scientific, Bremen, Germany) equipped with a nano-electrospray ionization source and FAIMS Pro interface (Thermo Scientific). Compensation voltages of -40 V, -60 V, and -75 V were used. Peptides were first loaded on a trapping column and subsequently separated inline on a 15 cm C18 column (75 µm x 15 cm, ReproSil-Pur 3 µm 120 Å C18-AQ, Dr. Maisch HPLC GmbH). The mobile phase consisted of water with 0.1% formic acid (solvent A) or acetonitrile/water (80:20 (v/v)) with 0.1% formic acid (solvent B). Peptides were eluted with the following gradient: from 5% to 21% of solvent B in 62 min, from 21% to 36% of solvent B in 48 min, from 36% to 100% of solvent B in 5 min, followed by 5 min at 100% of solvent B. MS data was acquired automatically by using Thermo Xcalibur 4.7 software (Thermo Fisher Scientific). Crosslinks were analyzed using the MS2-MS2-MS3 method where MS1 spectra were acquired in the Orbitrap mass analyzer with mass range of 375–1500 m/z at a resolution of 60,000. For the MS2-MS3-MS2 fragmentation method, sequential CID and ETD spectra were acquired for each precursor. MS3 scans were triggered by a targeted mass difference of 31.9721 detected in the MS2 scan. The MS3 scan was performed in the ion trap with CID fragmentation. Pairs of crosslinked peptides were identified by searching the raw data against the *S. africana* RNAP holoenzyme subunits using Proteome Discoverer 3.2 software (Thermo Scientific) and the XlinkX 3.2 algorithm (**Supplementary Data File**).

Table S1. Bacterial species employed in analysis presented in Figure 1. Related to Figure 1.

Kingdom	Superphylum	Phylum		Species
Pseudomonadati	Pseudomonadota and related phyla	Pseudomonadota	eco	*Escherichia coli*
			cvi	*Chromobacterium violaceum*
			rsp	*Cereibacter sphaeroides*
		Bdellovibrionota	bba	*Bdellovibrio bacteriovorus*
		Myxococcota	mxa	*Myxococcus xanthus*
		Thermodesulfobacteriota	gsu	*Geobacter sulfurreducens*
		Nitrospirota	nmv	*Nitrospira moscoviensis*
		Nitrospinota	tye	*Thermodesulfovibrio yellowstonii*
		Acidobacteriota	aca	*Acidobacterium capsulatum*
			nli	*Nitronauta litoralis*
	ACT	**A**quificota	aae	*Aquifex aeolicus*
			pmx	*Persephonella marina*
		Campylobacterota	tdn	*Sulfurimonas denitrificans*
			nap	*Nautilia sp. PV-1*
		Thermosulfidibacterota	ttk	*Thermosulfidibacter takaii*
	FCB+	**F**ibrobacterota	fsu	*Fibrobacter succinogenes*
		Gemmatimonadota	gau	*Gemmatimonas aurantiaca*
		Chlorobiota	cte	*Chlorobaculum tepidum*
		Bacteroidota	bth	*Bacteroides thetaiotaomicron*
		Rhodothermota	sru	*Salinibacter ruber*
		Balneolota	cprv	*Cyclonatronum proteinivorum Omega*
	PVC+	**P**lanctomycetota	rba	*Rhodopirellula baltica*
			hbs	*Humisphaera borealis*
		Kiritimatiellota	vbl	*Kiritimatiella glycovorans*
		Verrucomicrobiota	ote	*Opitutus terrae*
		Lentisphaerota	lpro	*Lentisphaera profundi*
		Chlamydiota	ctr	*Chlamydia trachomatis*
		Spirochaetota	sfc	*Spirochaeta africana*
			ock	*Oceanispirochaeta crateris*
			lbf	*Leptospira biflexa*
			taqu	*Thermospira aquatica*
Fusobacteriati		Fusobacteriota	fnu	*Fusobacterium nucleatum*
			haby	*Haliovirga abyssi*
Thermotogati	**DST**	**D**einococcota	dra	*Deinococcus radiodurans*
			ttj	*Thermus thermophilus*
		Synergistota	amo	*Acetomicrobium mobile*
			tai	*Thermanaerovibrio acidaminovorans*
		Thermotogota	tma	*Thermotoga maritima*
			mpg	*Mesotoga prima*
			tta	*Pseudothermotoga thermarum*
Bacillati		Cyanobacteriota	syn	*Synechocystis sp. PCC 6803*
			gvi	*Gloeobacter violaceus*
		Armatimonadota	ccz	*Chthonomonas calidirosea*
			fgi	*Fimbriimonas ginsengisoli*
		Chloroflexota	det	*Dehalococcoides mccartyi*
			tro	*Thermomicrobium roseum*
			cap	*Caldilinea aerophila*
		Actinomycetota	mtu	*Mycobacterium tuberculosis*
			sco	*Streptomyces coelicolor*
		Bacillota	bsu	*Bacillus subtilis*
			chy	*Carboxydothermus hydrogenoformans*
			dsy	*Desulfitobacterium hafniense*

Bold letters explain the names of superphyla

Table S2. Cryo-EM data collection, refinement and validation statistics.

	RPo (P-gre)				RPc (P-gre)	CarD-RPo (P-gre)	CarD-RPo (P-rrna)
State	Monomer I	Monomer II	Monomer III	Monomer IV	Dimer	Monomer I	Monomer
EMDB ID	56405	56406	56407	56408	56409	56410	56411
PDB ID	9TXX	9TXY	9TXZ	9TY0	9TY1	9TY2	9TY3
Data collection and processing							
Microscope	FEI Titan Krios G3i						
Voltage [keV]	300						
Camera	Falcon 3EC						
Magnification	96,000						
Pixel size at detector [Å/pixel]	0.832						
Total electron exposure [e^-/Å^2]	40						
Exposure rate [e^-/pixel/s]	0.7						
Frames per exposure	29						
Defocus range [µm]	0.5 - 2.5						
Automation software	EPU (version 2.8.1)						
Micrographs used	6,990				3,505	4,204	5,406
Total extracted particles	1,925,988				361,110	566,552	2,260,801
Final particles	163,995	52,968	70,566	47,627	90,219	56,632	394,310
Point-group or helical symmetry parameters	C1	C1	C1	C1	C2	C1	C1
Global resolution [Å]; $FSC_{0.143}$ (unmasked / masked)[a]	3.7 / 3	4.2 / 3.3	4.0 / 3.2	4.2 / 3.3	3.9 / 3.2	3.8 / 3.2	3.3 / 2.8
Local resolution range [Å]	2.4 - 38	2.5 - 40	2.5 - 40	2.6 - 40	2.5 - 40	2.6 - 43	2.2 - 40
Map sharpening *B* factor [Å^2] / *B* factor range	-91	-75	-83	-73	-85	-76	-94
Map sharpening method	Local *B* factor						
Refinement package	PHENIX (version 1.21_5419); real.space.refine						
Model composition							
Non-hydrogen atoms	30,517	31,358	31,235	31,269	61,999	32,315	32,097
Protein residues	3,578	3,658	3,646	3,643	3,436	3,753	3,764
Nucleic acid residues	102	110	112	115	145	124	109
Mg^{2+} ions	1	1	1	1	2	1	1
Zn^{2+} ions	2	2	2	2	4	2	2

Model Refinement							
Model-map scores							
CC[b] (mask)	0.86	0.86	0.85	0.78	0.85	0.75	0.86
CC (volume)	0.85	0.86	0.84	0.78	0.84	0.73	0.85
Average *B* factors [Å^2]							
Overall	154	216	191	183	157	125	140
Protein	146	211	170	177	154	120	125
Nucleic acid	264	276	459	252	220	182	348
Mg^{2+} ions	124	142	128	155	111	125	110
Zn^{2+} ions	142	162	144	162	154	92	125
Rmsd[c] from ideal values							
Bond lengths [Å]	0.003	0.003	0.003	0.003	0.003	0.003	0.003
Bond angles [°]	0.616	0.545	0.546	0.568	0.488	0.581	0.532
Validation[d]							
MolProbity score	2.07	2.15	2.15	2.22	2.09	2.02	1.69
CaBLAM outliers [%]	2.6	2.6	2.8	2.8	2.6	1.7	1.8
Clash score	11.6	11.3	11.6	12.4	10.8	9.9	8.7
Poor rotamers [%]	1.9	2.9	2.6	3.0	2.5	2.7	1.7
Cβ deviations	0	0	0	0	0	0	0
EMRinger score	2.05	2.10	2.01	2.02	2.46	2.48	2.97
Ramachandran plot							
Favored [%]	96.0	96.4	96.3	96.2	96.4	97.0	97.3
Allowed [%]	4.0	3.6	3.7	3.8	3.6	3.0	2.7
Outliers [%]	0	0	0	0	0	0	0
Ramach. *Z*-score (rmsd)							
Whole	0.57 (0.14)	0.69 (0.14)	0.78 (0.14)	0.62 (0.14)	0.81 (0.10)	0.95 (0.14)	1.26 (0.14)
Helix	1.85 (0.14)	1.91 (0.14)	1.85 (0.14)	1.83 (0.14)	1.86 (0.10)	1.72 (0.14)	2.05 (0.14)
Sheet	-0.30 (0.24)	-0.08 (0.25)	0.17 (0.25)	-0.12 (0.24)	0.11 (0.18)	0.41 (0.24)	0.61 (0.24)
Loop	-0.65 (0.15)	-0.61 (0.15)	-0.49 (0.15)	-0.60 (0.15)	-0.46 (0.10)	-0.22 (0.15)	-0.13 (0.15)

[a] FSC, Fourier shell correlation

[b] CC, correlation coefficient

[c] Rmsd, root-mean-square deviation

[d] Using MolProbity (PMID: 29067766)

Table S3. *E. coli* protein expression vectors used in this study. Related to STAR Methods.

Name	Description	protease	Source/reference
pVS10	wild-type *E. coli* RNAP (α-β-β'_his$_6$-ω)		[10]
pVS14	ΔSi3 *E. coli* RNAP (α-β-β'_his$_6$-ω)		[11]
pIP008	βS351N *E. coli* RNAP (α-his$_6$_β-β'-ω)		this work
pJM019	wild-type *S. africana* RNAP (α-β-β'_his$_6$-ω)		this work
pIP007	βN490S *S. africana* RNAP (α-his$_6$_β-β'_his$_6$-ω)		this work
pET-σ70	wild-type *E. coli* σ70 (his6_thrombin_σ70)	thrombin	[12]
pGB217	wild-type *S. africana* σ70 (his6_SUMO_σ70)	ULP1	this work
pGB179	*S. africana* CarD (his6_TEV_CarD)	TEV	this work
pGB175	*S. africana* DksA (his6_TEV_DksA)	TEV	this work
pRF2	*E. coli* DksA (his10_TEV_DksA)	TEV	[13]

Sequences of the plasmids are included in the **Supplemetary Data File**.

Table S4. Plasmids encoding transcription templates. Related to STAR Methods.

Name	Description	downstream gene in the genome	Source/reference
pOP004	P-gre with altered ITR	n/a	[14]
pVN003	P-rrna promoter	spiaf_2142, spiaf_2147, spiaf_2596	this work
pVN001	P-gre promoter	spiaf_1527	this work
pJK003	P-prs promoter	spiaf_1522	this work
pJK006	P-trna promoter	spiaf_0540	this work
pVL017	P-fla promoter	spiaf_1672	this work
pVL019	P-pori promoter	spiaf_0679	this work
pVL026	promoter-less	n/a	this work
pJK004	*E. coli* rrnB P1	*E. coli* rRNA genes (16S, 23S, 5S)	this work

Sequences of the plasmids are included in a **Supplemetary Data File**.

Supplementary references

1. Zhilina, T.N., Zavarzin, G.A., Rainey, F., Kevbrin, V.V., Kostrikina, N.A., and Lysenko, A.M. (1996). Spirochaeta alkalica sp. nov., Spirochaeta africana sp. nov., and Spirochaeta asiatica sp. nov., alkaliphilic anaerobes from the Continental Soda Lakes in Central Asia and the East African Rift. Int. J. Syst. Bacteriol. *46*, 305–312. 10.1099/00207713-46-1-305.

2. McClure, R., Balasubramanian, D., Sun, Y., Bobrovskyy, M., Sumby, P., Genco, C.A., Vanderpool, C.K., and Tjaden, B. (2013). Computational analysis of bacterial RNA-Seq data. Nucleic Acids Res. *41*, e140. 10.1093/nar/gkt444.

3. Liolos, K., Abt, B., Scheuner, C., Teshima, H., Held, B., Lapidus, A., Nolan, M., Lucas, S., Deshpande, S., Cheng, J.-F., et al. (2013). Complete genome sequence of the halophilic bacterium Spirochaeta africana type strain (Z-7692(T)) from the alkaline Lake Magadi in the East African Rift. Stand. Genomic Sci. *8*, 165–176. 10.4056/sigs.3607108.

4. Robinson, J.T., Thorvaldsdóttir, H., Winckler, W., Guttman, M., Lander, E.S., Getz, G., and Mesirov, J.P. (2011). Integrative genomics viewer. Nat. Biotechnol. *29*, 24–26. 10.1038/nbt.1754.

5. Langmead, B., and Salzberg, S.L. (2012). Fast gapped-read alignment with Bowtie 2. Nat. Methods *9*, 357–359. 10.1038/nmeth.1923.

6. Li, H., Handsaker, B., Wysoker, A., Fennell, T., Ruan, J., Homer, N., Marth, G., Abecasis, G., Durbin, R., and 1000 Genome Project Data Processing Subgroup (2009). The Sequence Alignment/Map format and SAMtools. Bioinformatics *25*, 2078–2079. 10.1093/bioinformatics/btp352.

7. Putri, G.H., Anders, S., Pyl, P.T., Pimanda, J.E., and Zanini, F. (2022). Analysing high-throughput sequencing data in Python with HTSeq 2.0. Bioinformatics *38*, 2943–2945. 10.1093/bioinformatics/btac166.

8. Okonechnikov, K., Golosova, O., Fursov, M., and UGENE team (2012). Unipro UGENE: a unified bioinformatics toolkit. Bioinformatics *28*, 1166–1167. 10.1093/bioinformatics/bts091.

9. Edgar, R.C. (2004). MUSCLE: multiple sequence alignment with high accuracy and high throughput. Nucleic Acids Res. *32*, 1792–1797. 10.1093/nar/gkh340.

10. Svetlov, V., and Artsimovitch, I. (2015). Purification of bacterial RNA polymerase: tools and protocols. Methods Mol. Biol. *1276*, 13–29. 10.1007/978-1-4939-2392-2_2.

11. Artsimovitch, I., Svetlov, V., Murakami, K.S., and Landick, R. (2003). Co-overexpression of Escherichia coli RNA polymerase subunits allows isolation and analysis of mutant enzymes lacking lineage-specific sequence insertions. J. Biol. Chem. *278*, 12344–12355. 10.1074/jbc.M211214200.

12. Marr, M.T., and Roberts, J.W. (1997). Promoter recognition as measured by binding of polymerase to nontemplate strand oligonucleotide. Science *276*, 1258–1260. 10.1126/science.276.5316.1258.

13. Furman, R., Danhart, E.M., NandyMazumdar, M., Yuan, C., Foster, M.P., and Artsimovitch, I. (2015). pH dependence of the stress regulator DksA. PLoS ONE *10*, e0120746. 10.1371/journal.pone.0120746.

14. Huang, Y.-H., Trapp, V., Puro, O., Mäkinen, J.J., Metsä-Ketelä, M., Wahl, M.C., and Belogurov, G.A. (2022). Fluorogenic RNA aptamers to probe transcription initiation and co-transcriptional RNA folding by multi-subunit RNA polymerases. Meth. Enzymol. *675*, 207–233. 10.1016/bs.mie.2022.07.010.

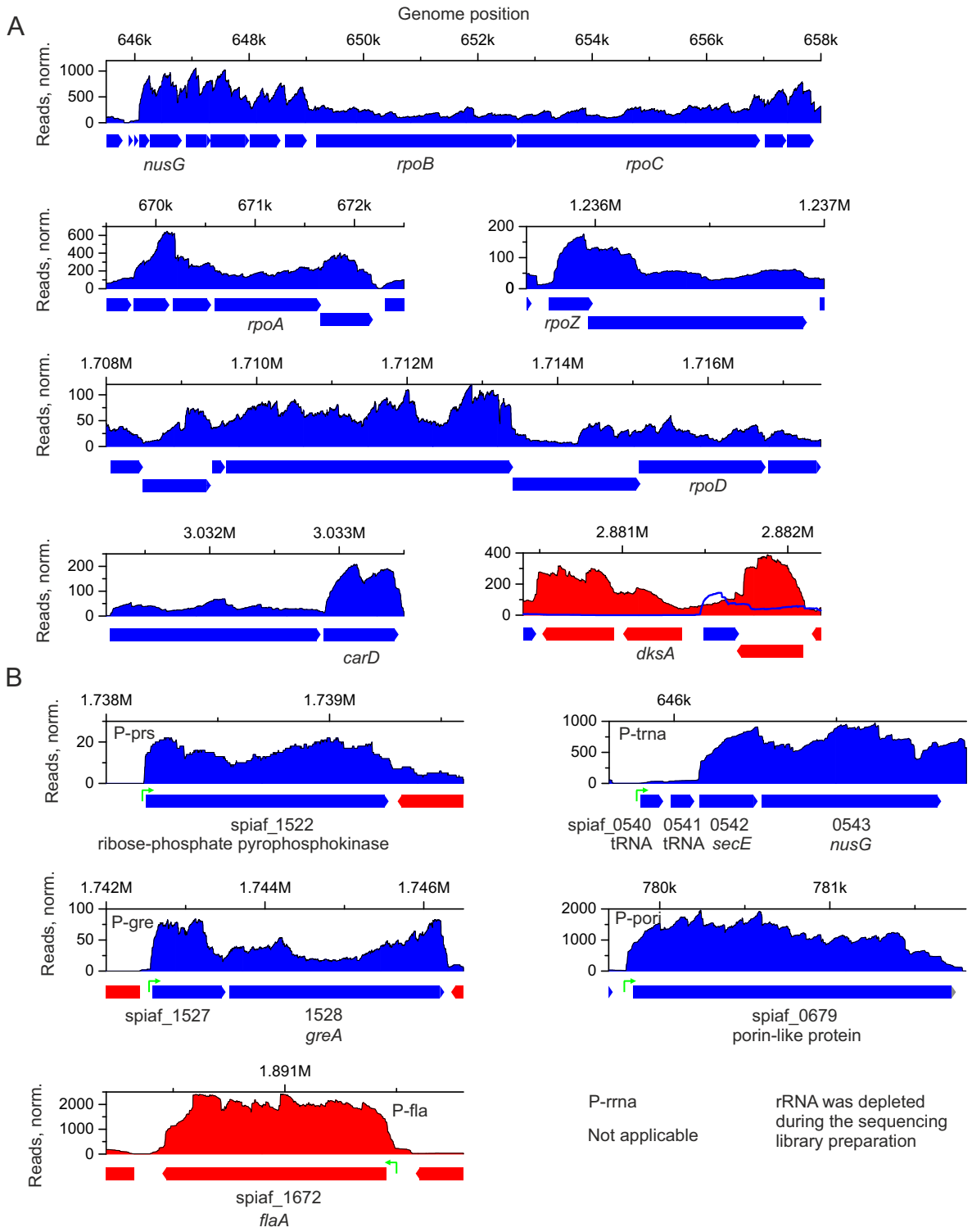

Figure S1. Strand-specific transcriptome coverage corresponding to the components of *S. africana* transcription system (A) and promoters investigated in this study (B). Related to **Figure 2**. Annotated genes are plotted below the transcriptome graphs. KEGG (www.kegg.jp) gene numbers (spiaf_xxxx) and selected gene names are indicated below the annotations. Coloring: positive strand coverage and annotations blue, negative strand coverage and annotations red.

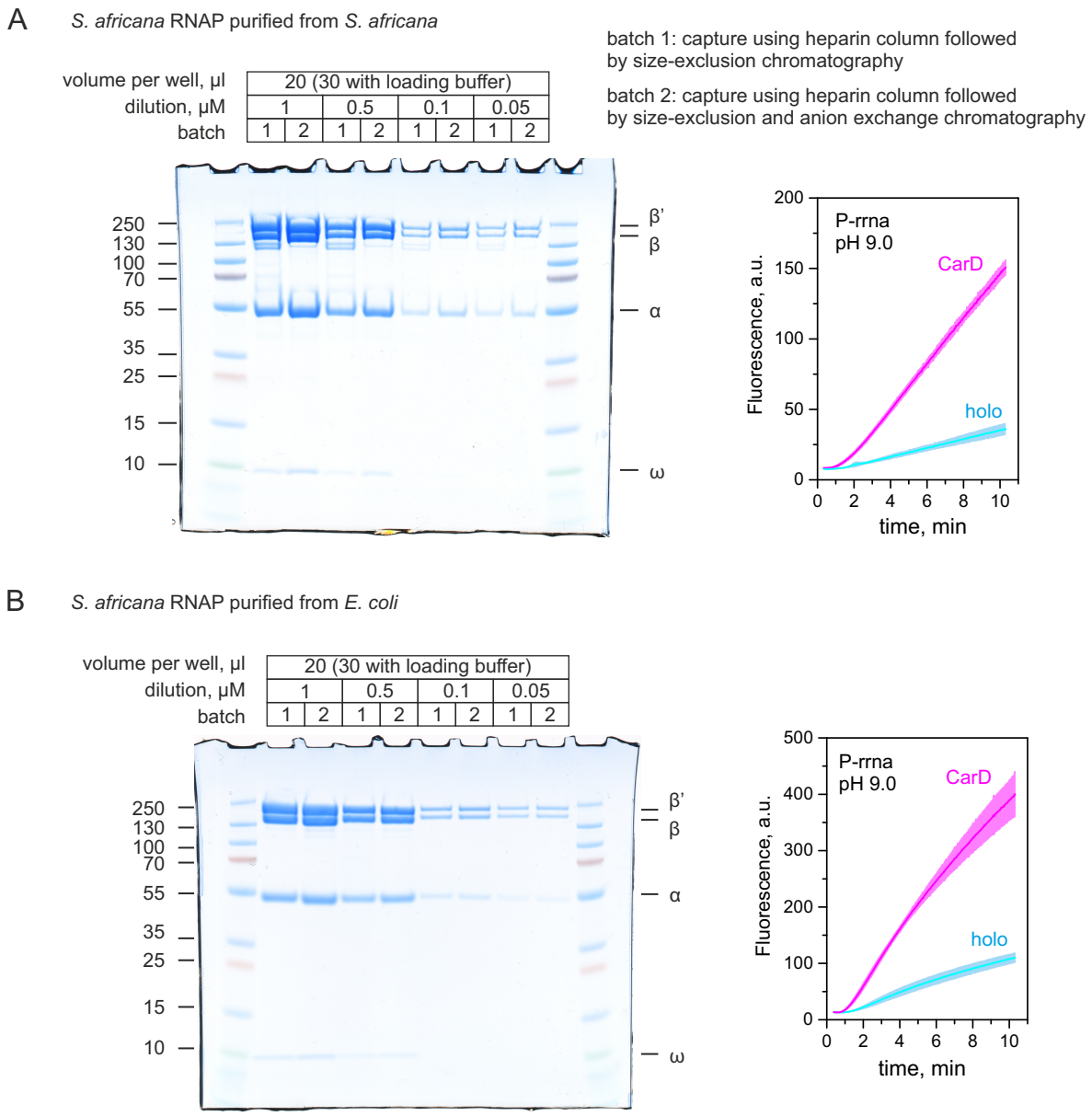

Figure S2. Transcriptional activity of *S. africana* RNAP purified from *S. africana* (A) and *E. coli* (B) at P-rrna promoter. Related to **Figure 2**. SDS-PAGE analysis was performed using the MES buffer system (50 mM MES, 50 mM Tris Base, 0.1% SDS, 1 mM EDTA, pH 7.3). Transcription activity was monitored using FLAP assay (1 µM RNAP, 4 µM σ, 50 nM DNA template and where indicated 10 µM CarD). Coloring: holoenzyme (cyan), in the presence of CarD (magenta). Promoter sequences and schematic of the FLAP assay are presented in the main text Figure 2.

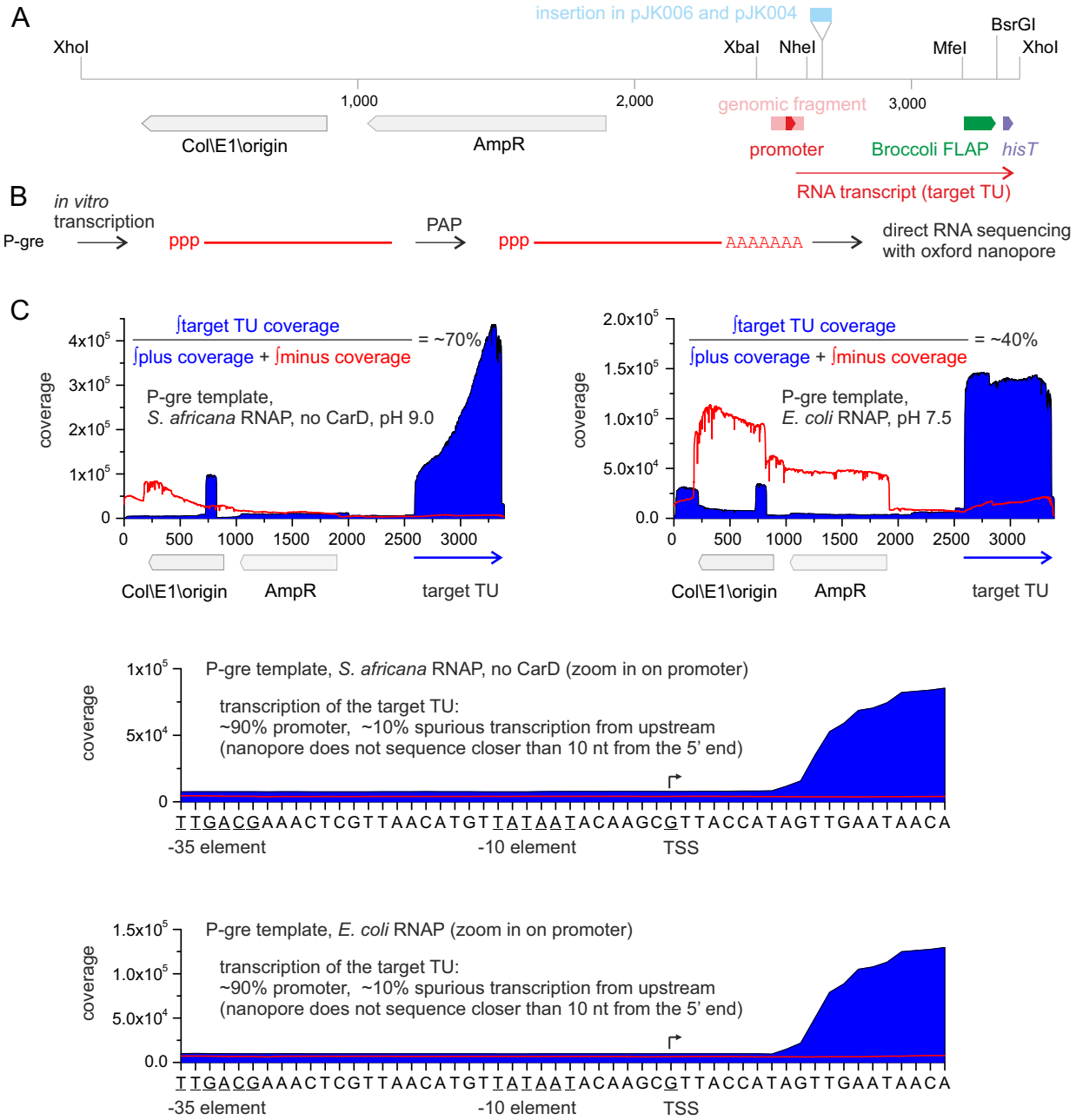

Figure S3. Analysis of RNA products transcribed by *S. africana* and *E. coli* holoenzymes from a linearized plasmid using direct RNA sequencing. Related to **Figure 2**. (A) Schematics of transcription templates used in this study. pVN001, pVN003, pJK003, pVL017, pVL019 and pOP005 plasmids differed only in the *Xba*I-*Nhe*I module containing plasmid-specific fragment of *S. africana* genome (pink) including the promoter (red). pJK006 additionally contained an insertion in the *Nhe*I-*Mfe*I module. *Mfe*I-*BsrG*I module encoded Broccoli FLAP embedded in tRNA scaffold, *BsrG*I-*Xho*I module encoded intrinsic transcription terminator. (B) Schematics of the experiment. *In vitro* transcription reactions (0.5 ml) were performed as in FLAP assays. Product RNA were purified using RNA easy kit (Qiagen), polyadenylated with *E. coli* poly-A polymerase (PAP). The sequencing library was prepared using Direct RNA sequencing kit (Oxford nanopore), and sequenced using MinION Mk1D instrument. (C) Reads were aligned to the P-gre transcription template using MinKNOW software, alignment files were split according to the strand using SAMtools, loaded into Ugene, per base coverage was exported and plotted using Origin software.

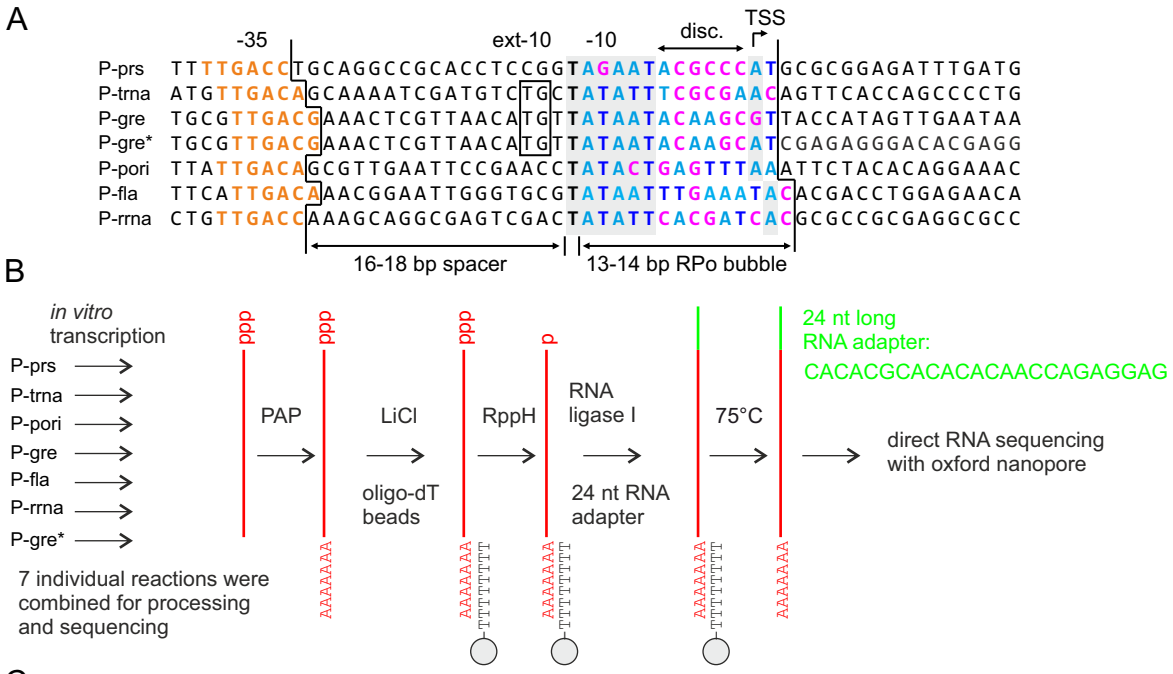

C

Search pattern	Read counts *Sfc*	*Eco*	
adapter P-prs			
GAGGAG GCGCGGA	0	7	TSS+2 or degradation
GAGGAG TGCGCGG	1	2	TSS+1 or degradation
GAGGAG ATGCGCG	**237**	**1525**	**TSS predicted**
GAGGAGCATGCGCG	2	0	TSS-1
adapter P-trna			
GAGGAG AGTTCAC	21	33	TSS+2 or degradation
GAGGAG CAGTTCA	0	7	TSS+1 or degradation
GAGGAG ACAGTTC	**609**	**1441**	**TSS predicted**
GAGGAG AACAGTTC	5	7	TSS-1
GAGGAG GAACAGTTC	1	1	TSS-2
GAGGAG CACAGTTC	2	6	slippage+degradation
GAGGAG ACACAGTTC	23	107	slippage
GAGGAGACACACAGTTC	1	1	slippage
adapter P-gre			
GAGGAG TTACCAT	22	1	TSS+1 or degradation
GAGGAG GTTACCA	**1365**	**375**	**TSS predicted**
GAGGAGCGTTACCA	4	1	TSS-1
adapter P-rrna			
GAGGAG CGCGCCG	2	0	TSS+1 or degradation
GAGGAG ACGCGCC	**172**	**228**	**TSS predicted**
GAGGAG CACGCGCC	61	131	TSS-1
GAGGAGTCACGCGCC	0	2	TSS-2

Search pattern	Read counts *Sfc*	*Eco*	
adapter P-pori			
GAGGAG ATTCTAC	16	1	TSS+2 or degradation
GAGGAG AATTCTA	31	12	TSS+1 or degradation
GAGGAG AAATTCT	**375**	**74**	**TSS predicted**
GAGGAG TAAATTCT	55	0	TSS-1
GAGGAG AAAATTCT	212	129	slippage
GAGGAG AAAAATTCT	25	29	slippage
GAGGAG AAAAAATTCT	6	3	slippage
GAGGAGAAAAAAATTCT	3	3	slippage
adapter P-fla			
GAGGAG ACGACCT	31	24	TSS+2 or degradation
GAGGAG CACGACC	17	7	TSS+1 or degradation
GAGGAG ACACGAC	**1868**	**755**	**TSS predicted**
GAGGAG TACACGAC	18	4	TSS-1
GAGGAG ATACACGAC	18	3	TSS-2
GAGGAG CACACGAC	5	2	slippage+degradation
GAGGAG ACACACGAC	129	86	slippage
GAGGAG ACACACACGAC	7	14	slippage
GAGGAGACACACACACGAC	0	1	slippage
adapter P-gre*			
GAGGAG AGAGGGA	1	4	TSS+4 or degradation
GAGGAG GAGAGGG	15	9	TSS+3 or degradation
GAGGAG CGAGAGG	15	6	TSS+2 or degradation
GAGGAG TCGAGAG	7	9	TSS+1 or degradation
GAGGAG ATCGAGA	**1763**	**2820**	**TSS predicted**
GAGGAGCATCGAGA	6	0	TSS-1

Figure S4. Transcription start site mapping using 5' adapter ligation followed by direct RNA sequencing. Related to **Figure 2.** (A) Promoter sequences used in this study aligned by -10 elements. Color coding as in main text **Figure 2**. (B) The schematics of *in vitro* RNA processing before sequencing. (C) Counts of reads that map to the adapter-RNA 5' end junction and contain indicated sequence patterns. RNAs were transcribed individually from 7 templates and combined for processing and sequencing. Separate sequencing runs were performed for *S. africana* and *E. coli* holoenzymes. Search patterns contain 6 nucleotides of the adapter and 7 nucleotides of RNA transcribed from the predicted TSS ±2 nucleotides. Additional patterns were designed after slippage was detected by manual inspection of read alignments. Patterns and read counts corresponding to the predicted TSS are indicated in bold text. RNA sequencing produced U-containing reads, but MinKNOW aligner converted U to T. Sequence patterns were then designed to feature T in place of U.

P-gre* promoter DNA (P-gre* = P-gre with an altered initially transcribed sequence):

```
5′-TCCCTGCCTGCGTTGACGAAACTCGTTAACATGTTATAATACAAGCATCGAGAGGGACACGAGGAA-3′
3′-AGGGACGGACGCAACTGCTTTGAGCAATTGTACAATATTATGTTCGTAGCTCTCCCTGTGCTCCTT-5′
```

Transcription bubble in P-gre TIC-CarD (unresolved nucleotides colored pink):

```
                                        ATAATACAAGCAT
5′-TCCCTGCCTGCGTTGACGAAACTCGTTAACATGTT              CGAGAGGGACACGAGGAA-3′
3′-AGGGACGGACGCAACTGCTTTGAGCAATTGTACAATATTATGTTCGTAGCTCTCCCTGTGCTCCTT-5′
```

Transcription bubble in P-gre TIC (unresolved nucleotides colored pink):

```
   state I
                                        ATAATACAAGCAT
5′-TCCCTGCCTGCGTTGACGAAACTCGTTAACATGTT              CGAGAGGGACACGAGGAA-3′
3′-AGGGACGGACGCAACTGCTTTGAGCAATTGTACAATATTATGTTCGTAGCTCTCCCTGTGCTCCTT-5′

   state II
                                        ATAATACAAGCAT
5′-TCCCTGCCTGCGTTGACGAAACTCGTTAACATGTT              CGAGAGGGACACGAGGAA-3′
3′-AGGGACGGACGCAACTGCTTTGAGCAATTGTACAATATTATGTTCGTAGCTCTCCCTGTGCTCCTT-5′

   state III
                                        ATAATACAAGCAT
5′-TCCCTGCCTGCGTTGACGAAACTCGTTAACATGTT              CGAGAGGGACACGAGGAA-3′
3′-AGGGACGGACGCAACTGCTTTGAGCAATTGTACAATATTATGTTCGTAGCTCTCCCTGTGCTCCTT-5′

   state IV
                                        ATAATACAAGCAT
5′-TCCCTGCCTGCGTTGACGAAACTCGTTAACATGTT              CGAGAGGGACACGAGGAA-3′
3′-AGGGACGGACGCAACTGCTTTGAGCAATTGTACAATATTATGTTCGTAGCTCTCCCTGTGCTCCTT-5′
```

P-rrna promoter DNA:

```
5′-CTTATAAAACCTTTTGATTTACTGTTGACCAAAGCAGGCGAGTCGACTATATTCACGATCACGCGCCGCGAGGCGCCGAT-3′
3′-GAATATTTTGGAAAACTAAATGACAACTGGTTTCGTCCGCTCAGCTGATATAAGTGCTAGTGCGCGGCGCTCCGCGGCTA-5′
```

Transcription bubble in P-rrna TIC-CarD (unresolved nucleotides colored pink):

```
                                                ATATTCACGATCAC
5′-CTTATAAAACCTTTTGATTTACTGTTGACCAAAGCAGGCGAGTCGACT              GCGCCGCGAGGCGCCGAT-3′
3′-GAATATTTTGGAAAACTAAATGACAACTGGTTTCGTCCGCTCAGCTGATATAAGTGCTAGTGCGCGGCGCTCCGCGGCTA-5′
```

Figure S5. Promoter scaffolds used to assemble *S. africana* holoenzyme - DNA complexes for cryoEM analysis. Related to **Figures 5-6**. Promoter elements are shaded in green. Nucleotides that were not represented by the density and omitted from structural models are shaded light pink.

σR1.1 Lys	-bridge-	other Lys	Max. XlinkX Score holo rep1	holo rep2	holo-CarD rep1	holo-CarD rep2	Location
K12	-DSSO-	β' K323	265	-	120	-	downstream DNA channel (Switch2)
K12	-DSSO-	β' K334	86	-	110	-	downstream DNA channel (Switch2)
K12	-DSSO-	σ K439	111	-	-	-	near upstream fork junction (σR3)
K12	-DSSO-	CarD K128	-	-	339	60	near upstream fork junction (CarD)
K18	-DSSO-	β'K323	76	84	65	-	downstream DNA channel (Switch2)
K18	-DSSO-	σ K51	182	-	171	-	σ1.1-σ1.1
K51	-DSSO-	β' K300	-	-	300	-	downstream DNA channel (Rudder)
K51	-DSSO-	β' K323	77	219	62	-	downstream DNA channel (Switch2)
K51	-DSSO-	β' K1150	144	184	-	-	downstream DNA channel (Jaw)
K51	-DSSO-	β' K1169	61	-	-	-	downstream DNA channel (Jaw)
K51	-DSSO-	β K800	110	-	-	-	near upstream fork junction (Flap)
K51	-DSSO-	β K1044	82	129	-	110	main channel (active site)
K51	-DSSO-	σ K18	182	-	171	-	σ1.1-σ1.1
K51	-DSSO-	σ K98	141	190	-	196	σ1.1-σ1.1
K51	-DSSO-	σ K173	138	211	-	118	near upstream fork junction (σNCR)
K51	-DSSO-	σ K369	78	-	-	-	near -10 element (σR2)
K51	-DSSO-	σ K395	191	183	236	144	near upstream fork junction (σR2)
K51	-DSSO-	σ K439	193	186	-	-	near upstream fork junction (σR3)
K51	-DSSO-	σ K472	-	-	-	238	near upstream fork junction (σR3)
K51	-DSSO-	CarD K128	-	-	65	-	near upstream fork junction (CarD)

holo = holoenzyme holo-CarD = holoenzyme with CarD DSSO = disuccinimidyl sulfoxide

Max. XlinkX Score represents the likelihood that a detected cross-linked peptide is a true positive identification. Crosslinks with the score >60 are considered reliable.

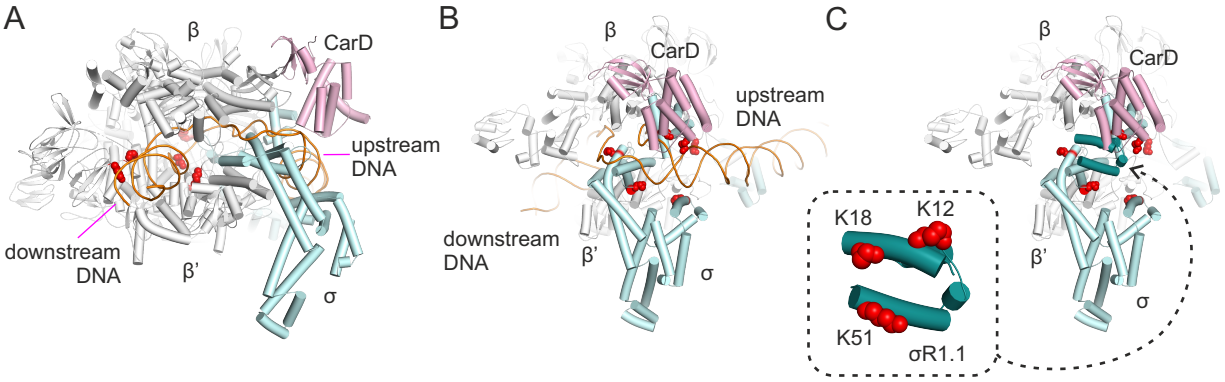

Figure S6. Probing the location of σR1.1 in *S. africana* holoenzyme by *in vitro* crosslinking with disuccinimidyl sulfoxide (DSSO) followed by mass spectrometry analysis. Related to **Figure 6**. Crosslinks involving Lys residues within the globular domain of σR1.1 (top table) were manually selected from the pool of all identified crosslinks (Supplementary Data File). Lys residues involved in crosslinks with σR1.1 lysines were then visualized (red spheres) on the structure of the *S. africana* RPo at the P-gre promoter with CarD. (A) σR1.1-crosslinkable Lys residues in Switch 2 region, the Rudder Loop and the Jaw domain suggest that σR1.1 is located in the downstream DNA channel. (B) σR1.1-crosslinkable Lys residues in σR2, σR3, σNCR and CarD suggest that σR1.1 is located in place of the upstream fork junction. (C) Same as in (B) but the promoter DNA was removed from the RPo structure and σR1.1 from the dimeric holoenzyme structure was modelled in using β subunit as a reference for structural alignment. The inset shows the zoomed in σR1.1 and σR1.1 Lys residues (red spheres) that form crosslinks discussed above.

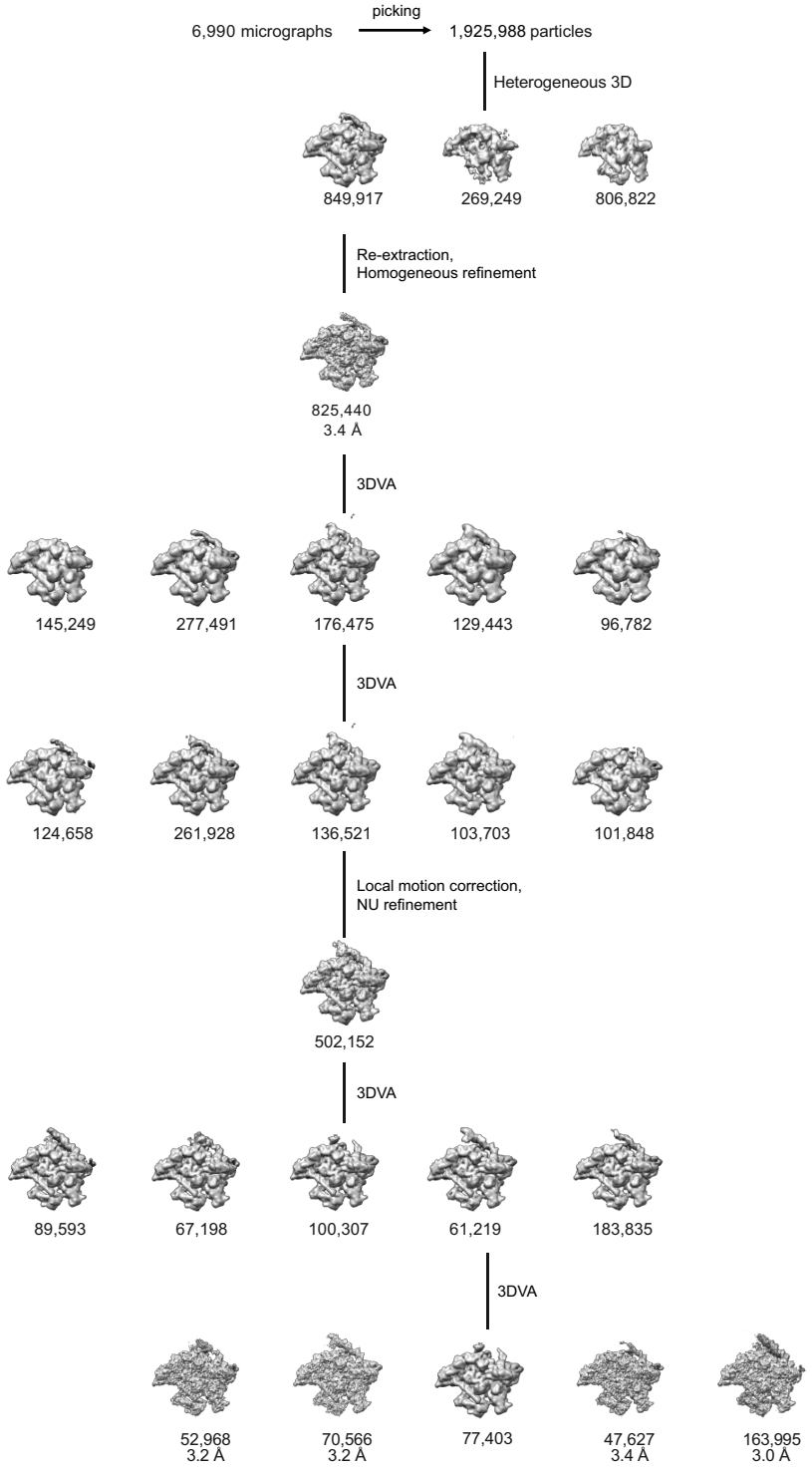

Figure S7. Hierarchical clustering analysis of particle images of monomeric *S. africana* holoenzyme-DNA complex assembled at P-gre promoter. Related to **Figure 5**.

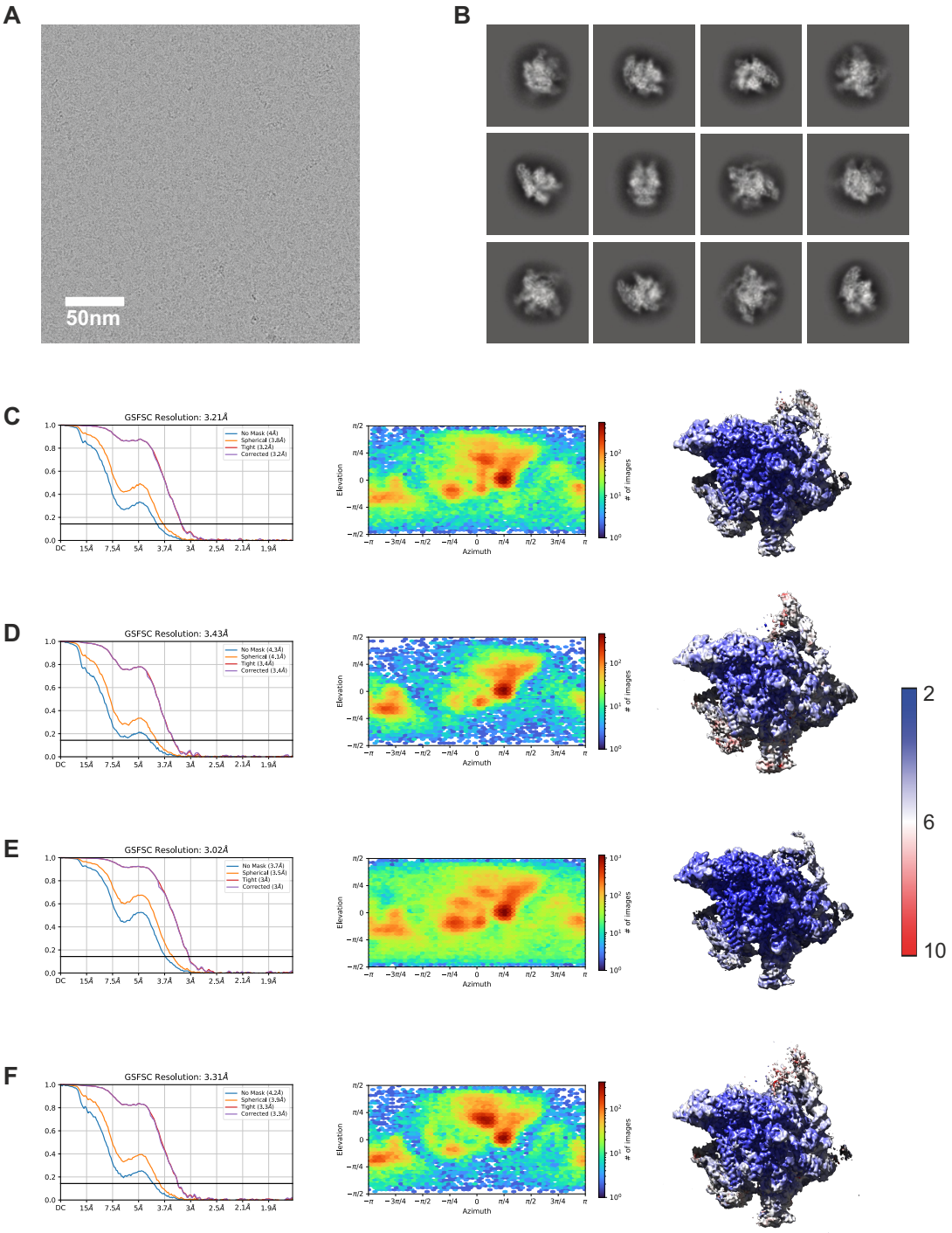

Figure S8. CryoEM data processing, monomeric *S. africana* holoenzyme-DNA complex assembled at P-gre promoter. Related to **Figure 5**. (A) Representative cryo-electron micrograph of the particles. Scale bar, 50 nm. (B) 2D class averages of the particle images. (C-F) Left, Fourier shell correlation (FSC) plots for half-maps of four states of the monomeric complex with 0.143 FSC criteria indicated; nominal resolutions 3.2 Å, 3.4 Å, 3.0 Å and 3.3 Å. Middle, the distributions of particle orientations show preferential orientation bias. Right, local resolution plots.

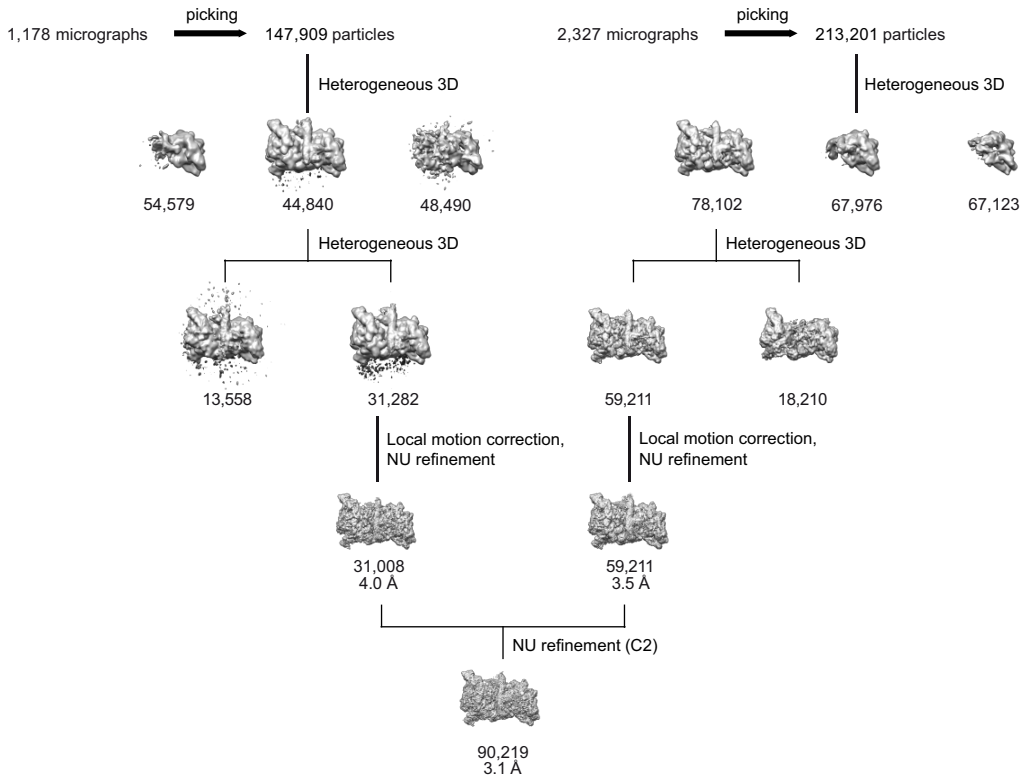

Figure S9. Hierarchical clustering analysis of particle images of dimeric *S. africana* holoenzyme-DNA complex assembled at P-gre promoter. Related to **Figure** 6.

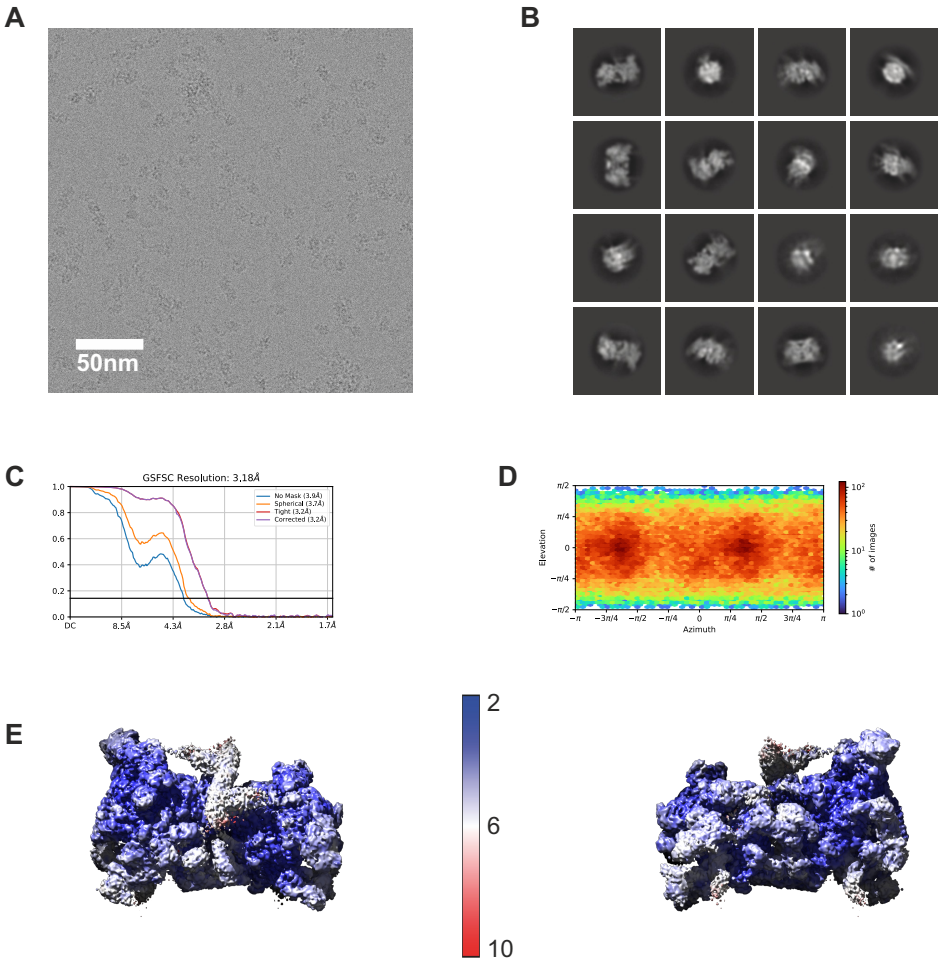

Figure S10. CryoEM data processing, dimeric *S. africana* holoenzyme-DNA complex assembled at P-gre promoter DNA. Related to **Figure 6**. (A) Representative cryo-electron micrograph of the particles. Scale bar, 50 nm. (B) 2D class averages of the particle images. (C) Fourier shell correlation (FSC) plot for half-maps of the dimeric complex with 0.143 FSC criteria indicated; nominal resolution 3.2 Å. (D) The distribution of particle orientations shows preferential orientation bias. (E) Local resolution plots.

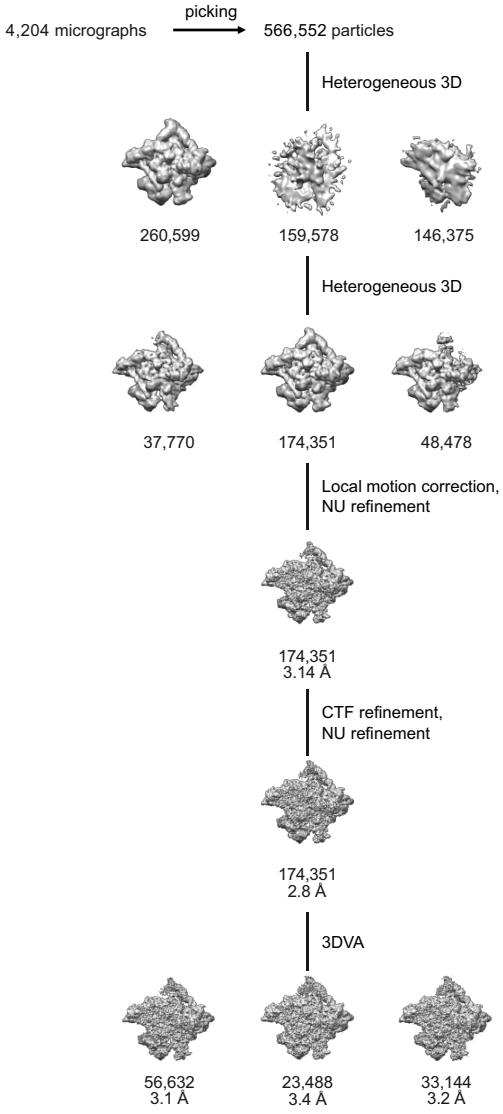

Figure S11. Hierarchical clustering analysis of particle images of CarD-modified *S. africana* holoenzyme-DNA complex assembled at P-gre promoter. Related to **Figure 5**.

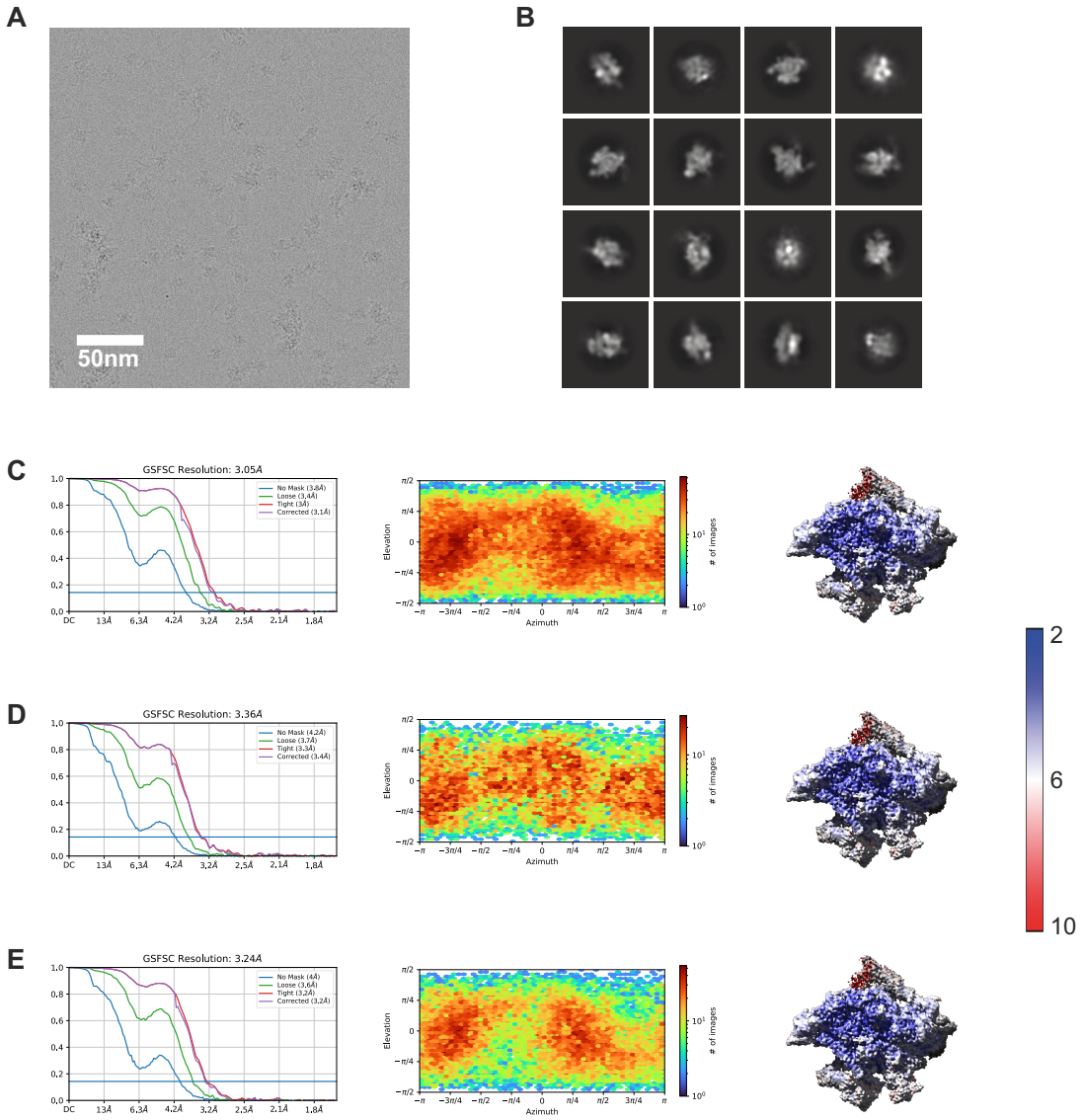

Figure S12. CryoEM data processing, CarD-modified *S. africana* holoenzyme-DNA complex assembled at P-gre promoter. Related to **Figure 5**. (A) Representative cryo-electron micrograph of the particles. Scale bar, 50 nm. (B) 2D class averages of the particle images. (C-E) Left, Fourier shell correlation (FSC) plots for half-maps of three states of the complex with 0.143 FSC criteria indicated; nominal resolutions 3.0 Å, 3.3 Å and 3.2 Å. Middle, the distributions of particle orientations show preferential orientation bias. Right, local resolution plots.